

Graphene: Junctions and STM Spectra

M. Maiti

*The Institute of Mathematical Sciences,
C.I.T Campus Taramani, Chennai-600113, India.*

K. Saha and K. Sengupta

*Theoretical Physics Department, Indian Association
for the Cultivation of Science, Kolkata-700032, India.*

I. INTRODUCTION

Graphene, a two-dimensional single layer of graphite, was first fabricated in 2004 by Novoselov *et. al.*¹. This has provided an unique opportunity for experimental observation of electronic properties of graphene which has attracted theoretical attention for several decades². The importance of graphene lies not only in providing the first realization of Dirac physics in condensed matter systems but also in providing a way of realization of several devices in nanometer scale. In this article, we are going to concern ourselves mainly on the first of these two aspects of graphene.

In graphene, the energy bands touch the Fermi energy at six discrete points at the edges of the hexagonal Brillouin zone. Out of these six Fermi points, only two are inequivalent; they are commonly referred to as K and K' points³. The quasiparticle excitations about these K and K' points obey linear Dirac-like energy dispersion. The presence of such Dirac-like quasiparticles is expected to lead to a number of unusual electronic properties in graphene including relativistic quantum Hall effect with unusual structure of Hall plateaus⁴. Recently, experimental observation of the unusual plateau structure of the Hall conductivity has confirmed this theoretical prediction⁵. Further, as suggested in Ref. 6, the presence of such quasiparticles in graphene provides us with an experimental test bed for Klein paradox.⁷ These and several other properties of graphene has been covered extensively in several review articles⁸⁻¹⁰. In the current article, we are going to focus on the effect of the Dirac nature of graphene quasiparticles on two separate aspects. The first of these involves transport of superconducting graphene junctions while the second involves Kondo effect and scanning tunneling spectra of graphene.

It is well known that the existence Dirac-like quasiparticles affects tunneling conductance of a normal metal-superconductor (NS) interface of graphene¹¹. Graphene is not a natural superconductor. However, superconductivity can be induced in a graphene layer in the presence of a superconducting electrode near it via proximity effect¹¹⁻¹³ or by possible intercalation with dopant molecules¹⁴. It has been recently predicted¹¹ that a graphene NS junction, due to the Dirac-like energy spectrum of its quasiparticles, can exhibit specular Andreev reflection in contrast to the usual retro reflection observed in conventional NS junctions^{15,16}. Such specular Andreev reflection process leads to qualitatively different tunneling conductance curves compared to conventional NS junctions¹¹. The effect of the

presence of a thin barrier region of thickness $d \rightarrow 0$ created by applying a large gate voltage $V_0 \rightarrow \infty$ (such that $V_0 d$ is finite) between the normal and the superconducting region has also been studied in Ref. 17. It has been shown that in this thin barrier limit, in contrast to all normal metal-barrier-superconductor (NBS) junctions studied so far, the tunneling conductance of a graphene NBS junction is an oscillatory function of the dimensionless barrier strength $\chi = V_0 d / (\hbar v_F)$, where v_F denotes the Fermi velocity of graphene, with periodicity π . Further, it has also been demonstrated that the tunneling conductance reaches its maxima of $2G_0$ for $\chi = (n + 1/2)\pi$, where n is an integer. The latter result was also interpreted in terms of transmission resonance property of the Dirac-Bogoliubov quasiparticles⁵. However, no such studies have been undertaken for NBS junctions with barriers of arbitrary thickness d and barrier potential V_0 . As we shall discuss in details in Sec. II A, the analysis of Ref. 17 and calculate the tunneling conductance of a graphene NBS junction with a barrier of thickness d and with an arbitrary voltage V_0 applied across the barrier region can also be extended to thick barrier junctions¹⁸. It can be shown that the oscillatory behavior of the tunneling conductance is not a property of the thin barrier limit, but persists for arbitrary barrier width d and applied gate voltage V_0 , as long as $d \ll \xi$, where ξ is the coherence length of the superconductor. Further, the periodicity and amplitude of these oscillations deviate from their values in the thin barrier limit and becomes a function of the applied voltage V_0 .

The study of Josephson effect in graphene for tunnel SBS junctions also presents some unconventional features due to the presence of the Dirac quasiparticles. In this review, we shall concentrate on SBS junctions with barrier thickness $d \ll \xi$ where ξ is the superconducting coherence length, and width L which has an applied gate voltage V_0 across the barrier region¹⁹. The central property of such junctions on which we shall mainly focus on is that in complete contrast to the conventional Josephson tunnel junctions studied so far^{20,21}, the Josephson current in graphene SBS tunnel junctions is an oscillatory function of both the barrier thickness d and the applied gate voltage V_0 . In the thin barrier limit, where the barrier region can be characterized by an effective dimensionless barrier strength $\chi = V_0 d / \hbar v_F$ (v_F being the Fermi velocity of electrons in graphene), the Josephson current becomes an oscillatory function of χ with period π ¹⁹. In this limit, the oscillatory behavior of Josephson current can be understood as a consequence of transmission resonance phenomenon of Dirac-Bogoliubov-de Gennes (DBdG) quasiparticles in graphene. The Josephson current reaches

the Kulik-Omelyanchuk limit²² for $\chi = n\pi$ (n being an integer), but, unlike conventional junctions, never reaches the Ambegaokar Baratoff limit²³ for large χ . This analysis is done in Sec. II B.

Another extremely interesting phenomenon in conventional metal systems is the Kondo effect which occurs in the presence of dilute concentration of localized quantum spins coupled to the spin-degenerate Fermi sea of metal electrons²⁴. The impurity spin-electron interaction then results in perfect or partial screening of the impurity spin as one approaches zero temperature. It also results in a sharp ‘Kondo Resonance’ in electron spectral functions. Recent developments in quantum dots and nano devices have given new ways in which various theoretical results in Kondo physics, which are not easily testable otherwise, can be tested and confirmed experimentally²⁵. Most of the early studies in Kondo effect were carried on for conventional metallic systems with constant density of states (DOS) at the Fermi surface²⁶. Some studies on Kondo effect in possible flux phases²⁷, nodal quasiparticles in d-wave superconductors²⁸, Luttinger liquids²⁹, and hexagonal Kondo lattice³⁰, for which the DOS of the associated Fermions vanishes as some power law at the Fermi surface, has also been undertaken. Recently, there has been a interest in study of the physics of magnetic impurities in graphene.^{31–35} One of the purpose of this article is to articulate a part of this recent progress in Sec. IV A.

Scanning tunneling microscopes (STM) are extremely useful probes for studying properties of two or quasi-two dimensional materials^{36,37}. Studying electronic properties of a sample with STM typically involves measurement of the tunneling conductance $G(V)$ for a given applied voltage V . The tunneling conductances measured in these experiments have also been studied theoretically for conventional metallic systems and are known to exhibit Fano resonances at zero bias voltage in the presence of impurities^{38,39}. The application and utility of this experimental technique, with superconducting STM tips, has also been discussed in the literature for conventional systems⁴⁰. However, tunneling spectroscopy of graphene using superconducting STM tips remains to be studied both experimentally and theoretically. In Sec. IV B, we shall elaborate the progress on the STM response of doped graphene and discuss some of it’s unconventional features. For undoped graphene with Fermi energy $E_F = 0$, the derivative of the STM tunneling conductance (G) with respect to the applied voltage (dG/dV) reflects the density of states (DOS) of the STM tip (ρ_t), *i.e.*, $dG/dV \sim +(-)\rho_t$ for $V > (<)0$. By tuning E_F , one can interpolate between this

unconventional $\rho_t \sim \pm dG/dV$ and the conventional $\rho_t \sim G$ (seen for $E_F \gg eV$) behaviors. Further, for superconducting STM tips with energy gap Δ_0 , $G(dG/dV)$ displays a cusp (discontinuity) at $eV = -E_F - \Delta_0$ as a signature of the Dirac point which should be experimentally observable in graphene with small E_F where the regime $eV > E_F$ can be easily accessed. For impurity doped graphene with large E_F , experiments in Ref. 35 have seen that the tunneling conductance, as measured by a metallic STM tip, depends qualitatively on the position of the impurity in the graphene matrix. For impurity atoms atop the hexagon center, the zero-bias tunneling conductance shows a peak; for those atop a graphene site, it shows a dip. We provide a detailed discussion of this phenomenon and point out that its origin lies in conservation/breaking of pseudospin symmetry of the Dirac quasiparticles by the impurity.

The organization of the rest of the review is as follows. We give a generic description of the graphene NBS and SBS tunnel junctions which is described by the Dirac-Bogoliubov-de Gennes (DBdG) equations. In section II A we review the theory of tunneling conductance of a graphene NBS junction with a barrier of thickness d and with an arbitrary voltage V_0 applied across the barrier region. The results obtained are then compared and contrasted with that of a thin barrier and zero barrier junction. In section II B we study Josephson current for a general SBS junction barrier region of thickness d and potential V_0 . We also discuss the thin barrier limit to understand the oscillatory behavior in terms of transmission resonance of DBdG particles. Finally we study some possible experimental realizations of the above mentioned junctions to probe the oscillations in section III. In section. IV A, we discuss the unconventional Kondo effect in graphene. We describe the large N analysis for a generic spin S local moment coupled to Dirac electrons in graphene. The analysis gives rise to a finite critical Kondo coupling strength which can be tuned by the application of an external gate voltage and is particular to graphene. We also discuss the possible realization of the non-Fermi liquid ground states via the multichannel Kondo effect. In section IV B, we discuss the STM response of graphene. We discuss the tunneling current through the STM tip within linear-response theory using a superconducting tip to probe an undoped sample and a metallic tip with constant density of states (DOS) to probe an impurity present in the sample. We conclude with a general discussion on the unconventional tunneling, STM properties and the behaviour of magnetic impurities in graphene in section V.

II. TRANSPORT PROPERTIES OF SUPERCONDUCTING JUNCTIONS

An understanding of the transport properties across different superconducting junctions of graphene throws substantial light on the electronic properties. A generic description of the junctions to study the transport properties is as follows. A local potential barrier of width d is implemented on the graphene sheet occupying the xy plane by either using the electric field effect or local chemical doping^{5,6,41}. A s -wave pairing $\Delta(\mathbf{r})$ is induced in graphene via proximity effect^{11,42}. For NBS (SBS) region **I** is normal (superconducting) region occupying $x \leq d$ for all y as shown schematically in Fig. 1. The region **II** modeled by a barrier potential V_0 , extends from $x = d$ to $x = 0$ while the superconducting region occupies $x \geq 0$ (marked as region **III** in Fig (1)). For calculations we shall assume that the barrier region has sharp edges on both sides. This condition requires that $d \ll \lambda = 2\pi/k_F$, where k_F and λ are Fermi wave-vector and wavelength for graphene, and can be realistically created in experiments⁶. Also, the interface is smooth and impurity free on the scale of the superconducting coherence length $\xi = \hbar v_F/\Delta_0$, where Δ_0 is the amplitude of the induced superconducting order parameter. For both the junctions (NBS and SBS) the induced pair potential can be modeled (with appropriate boundary condition for the two different junctions) as:

$$\Delta(\mathbf{r}) = \Delta_0 \exp(i\phi) \quad (1)$$

ϕ is the phase. These junctions can then be described by the Dirac-Bogoliubov-de Gennes (DBdG) equations:

$$\begin{pmatrix} \mathcal{H}_a - E_F + U(\mathbf{r}) & \Delta(\mathbf{r}) \\ \Delta^*(\mathbf{r}) & E_F - U(\mathbf{r}) - \mathcal{H}_a \end{pmatrix} \psi_a = E \psi_a \quad (2)$$

Here, $\psi_a = (\psi_{Aa}, \psi_{Ba}, \psi_{A\bar{a}}^*, -\psi_{B\bar{a}}^*)$ are the 4 component wavefunctions for the electron and hole spinors, the index a denote K or K' for electron/holes near K and K' points, \bar{a} takes values $K'(K)$ for $a = K(K')$, E_F denote the Fermi energy. A and B denote the two inequivalent sites in the hexagonal lattice of graphene, and the Hamiltonian \mathcal{H}_a is given by

$$\mathcal{H}_a = -i\hbar v_F (\sigma_x \partial_x + \text{sgn}(a) \sigma_y \partial_y). \quad (3)$$

In Eq. 3, v_F denotes the Fermi velocity of the quasiparticles in graphene and $\text{sgn}(a)$ takes values \pm for $a = K(K')$. The potential $U(\mathbf{r})$ gives the relative shift of Fermi energies in the

barrier and superconducting regions and is modeled as:

$$U(\mathbf{r}) = V_0 \theta(-x) \theta(x + d) \quad (4)$$

Eq. 2 can be solved in a straightforward manner to yield the wavefunction ψ in the normal, insulating and the superconducting regions, taking into account both Andreev and normal reflection processes. These wavefunctions satisfy the appropriate boundary conditions at the interfaces of the junctions. Note however that these boundary conditions, in contrast their counterparts in standard junction interfaces, do not impose any constraint on derivative of the wavefunctions at the boundary. The tunneling conductance and Josephson current across the junctions can then be calculated using appropriate expressions. These are found to have novel oscillatory behavior in complete contrast to their standard counterparts as will be described in the subsequent sections.

A. NBS junction

The pair-potential for the NBS junction is modeled as:

$$\Delta(\mathbf{r}) = \Delta_0 \exp(i\phi) \theta(x), \quad (5)$$

$\theta(x)$ is the Heaviside step function. Eq. 2 can be solved in a straightforward manner to yield the wavefunction ψ in the normal, insulating and the superconducting regions. In the normal region, for electron and holes traveling the $\pm x$ direction with a transverse momentum $k_y = q$ and energy ϵ , the (unnormalized) wavefunctions are given by

$$\begin{aligned} \psi_N^{e\pm} &= (1, \pm e^{\pm i\alpha}, 0, 0) \exp[i(\pm k_n x + qy)], \\ \psi_N^{h\pm} &= (0, 0, 1, \mp e^{\pm i\alpha'}) \exp[i(\pm k'_n x + qy)], \\ \sin(\alpha) &= \frac{\hbar v_F q}{\epsilon + E_F}, \quad \sin(\alpha') = \frac{\hbar v_F q}{\epsilon - E_F}, \end{aligned} \quad (6)$$

where the wave-vector $k_n(k'_n)$ for the electron (hole) wavefunctions are given by

$$k_n(k'_n) = \sqrt{\left(\frac{\epsilon + (-)E_F}{\hbar v_F}\right)^2 - q^2}, \quad (7)$$

and $\alpha(\alpha')$ is the angle of incidence of the electron (hole).

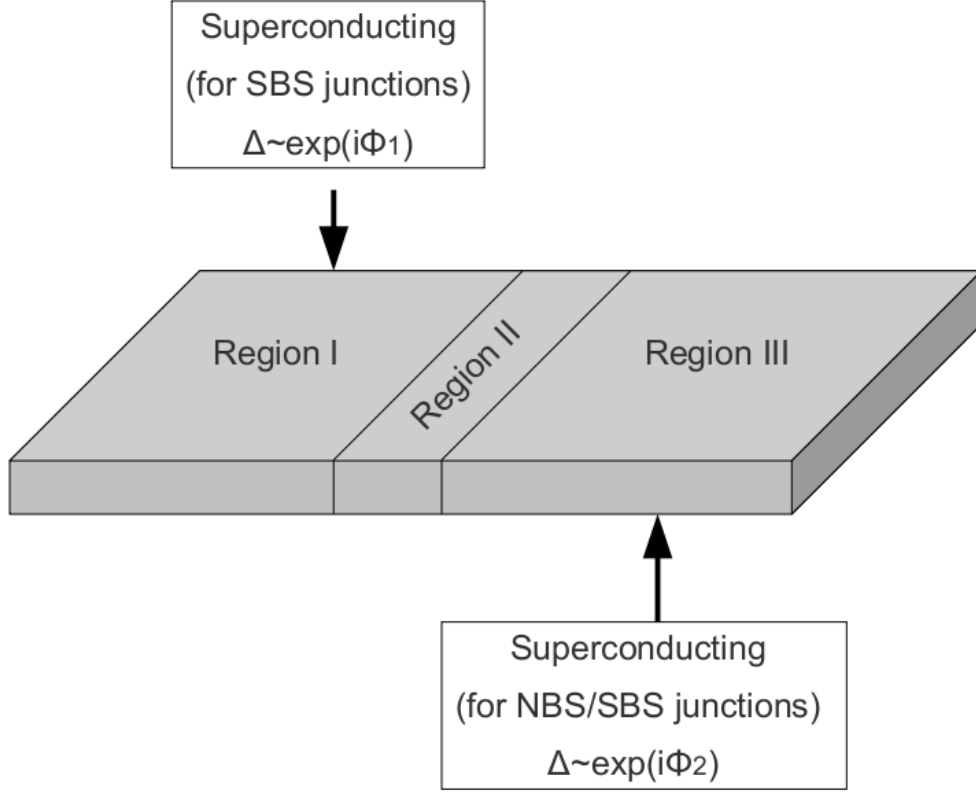


FIG. 1. A schematic sketch of the graphene superconducting junction. Region I denotes the normal(superconducting) region for NBS(SBS) junction. A potential barrier V_0 of width d is created with the application of the external gate voltage. The region III is the superconducting region for both the NBS and SBS junctions. Superconductivity, as discussed in the text is induced in the graphene layer by proximity effect.

In the barrier region, one can similarly obtain

$$\begin{aligned}\psi_B^{e\pm} &= (1, \pm e^{\pm i\theta}, 0, 0) \exp[i(\pm k_b x + qy)], \\ \psi_B^{h\pm} &= (0, 0, 1, \mp e^{\pm i\theta'}) \exp[i(\pm k'_b x + qy)],\end{aligned}\quad (8)$$

for electron and holes moving along $\pm x$. Here the angle of incidence of the electron(hole) $\theta(\theta')$ and the wavevector $k_b(k'_b)$ are given by is

$$\begin{aligned}\sin[\theta(\theta')] &= \hbar v_F q / [\epsilon + (-)(E_F - V_0)], \\ k_b(k'_b) &= \sqrt{\left(\frac{\epsilon + (-)(E_F - V_0)}{\hbar v_F}\right)^2 - q^2}.\end{aligned}\quad (9)$$

Note that Eq. 8 ceases to be the solution of the Dirac equation (Eq. 2) when $E_F = V_0$ and $\epsilon = 0$. For these parameter values, Eq. 2 in the barrier region becomes $\mathcal{H}_a\psi_B = 0$ which do not have purely oscillatory solutions. For the rest of the calculation, we shall restrict ourselves to the regime $V_0 > E_F$.

In the superconducting region, the DBdG quasiparticles are mixtures of electron and holes. Consequently, the wavefunctions of the DBdG quasiparticles moving along $\pm x$ with transverse momenta q and energy ϵ , for $(U_0 + E_F) \gg \Delta_0, \epsilon$, has the form

$$\psi_I^\pm = (w_1^\pm, w_2^\pm, w_3^\pm, w_4^\pm) e^{[i(\pm k_s x + qy) + \kappa x]} \quad (10)$$

where

$$\begin{aligned} \frac{w_2^\pm}{w_1^\pm} &= \pm \exp(\pm i\gamma), & \frac{w_3^\pm}{w_1^\pm} &= \exp[-i(\phi_1 \mp \beta)], \\ \frac{w_4^\pm}{w_1^\pm} &= \pm \exp[\pm i(\mp \phi_1 + \beta + \gamma)], \end{aligned} \quad (11)$$

where γ is the angle of incidence for the quasiparticles. Here the wavevector k_s and the localization length κ^{-1} can be expressed as a function of the energy ϵ and the transverse momenta q as

$$\begin{aligned} k_s &= \sqrt{[(U_0 + E_F) / \hbar v_F]^2 - q^2}, \\ \kappa^{-1} &= \frac{(\hbar v_F)^2 k_s}{[(U_0 + E_F) \Delta_0 \sin(\beta)]}, \end{aligned} \quad (12)$$

where β is given by

$$\begin{aligned} \beta &= \cos^{-1}(\epsilon / \Delta_0) \quad \text{if } |\epsilon| < \Delta_0, \\ &= -i \cosh^{-1}(\epsilon / \Delta_0) \quad \text{if } |\epsilon| > \Delta_0. \end{aligned} \quad (13)$$

Note that for $|\epsilon| > \Delta_0$, κ becomes imaginary and the quasiparticles can propagate in the bulk of the superconductor.

Next we note that for the Andreev process to take place, the angles θ , θ' and α' must all be less than 90° . This sets the limit of maximum angle of incidence α . Using Eqns. 6 and 9, one finds that the critical angle of incidence is

$$\begin{aligned} \alpha_c &= \alpha_c^{(1)} \theta(V_0 - 2E_F) + \alpha_c^{(2)} \theta(2E_F - V_0) \\ \alpha_c^{(1)} &= \arcsin[|\epsilon - E_F| / (\epsilon + E_F)], \\ \alpha_c^{(2)} &= \arcsin[|\epsilon - |E_F - V_0|| / (\epsilon + E_F)]. \end{aligned} \quad (14)$$

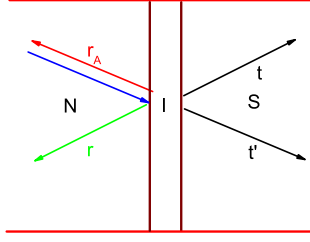


FIG. 2. A schematic sketch of normal reflection (r), Andreev reflection (r_A) and transmission processes (t and t') at a graphene NBS junction. Note that in this schematic picture, we have chosen r_A to denote a retro Andreev reflection for illustration purpose. In practice, as discussed in the text, r_A takes into account possibilities of both retro and specular Andreev reflections. The electron and hole wavefunctions inside the barrier region is not sketched to avoid clutter.

Note that in the thin or zero barrier limits treated in Refs. 17 and 11, $\alpha_c = \alpha_c^{(1)}$ for all parameter regimes.

Let us now consider a electron-like quasiparticle incident on the barrier from the normal side with an energy ϵ and transverse momentum q . The basic process of ordinary and Andreev reflection that can take place at the interface is schematically sketched in Fig. 2. As noted in Ref. 11, in contrast to conventional NBS junction, graphene junctions allow for both retro and specular Andreev reflections. The former dominates when $\epsilon, \Delta_0 \ll E_F$ so that $\alpha = -\alpha'$ (Eq. 6) while that latter prevails when $E_F \ll \epsilon, \Delta_0$ with $\alpha = \alpha'$. Note that in Fig. 2, we have chosen r_A to denote a retro Andreev reflection for illustration purposes. In practice, r_A includes both retro and specular Andreev reflections. In what follows, we shall denote the total probability amplitude of Andreev reflection as r_A which takes into account possibilities of both retro and specular Andreev reflections.

The wave functions in the normal, insulating and superconducting regions, taking into account both Andreev and normal reflection processes, can then be written as¹⁶

$$\begin{aligned}\Psi_N &= \psi_N^{e+} + r\psi_N^{e-} + r_A\psi_N^{h-}, & \Psi_S &= t\psi_S^+ + t'\psi_S^-, \\ \Psi_B &= p\psi_B^{e+} + q\psi_B^{e-} + m\psi_B^{h+} + n\psi_B^{h-},\end{aligned}\tag{15}$$

where r and r_A are the amplitudes of normal and Andreev reflections respectively, t and t' are the amplitudes of electron-like and hole-like quasiparticles in the superconducting

region and p , q , m and n are the amplitudes of electron and holes in the barrier. These wavefunctions must satisfy the appropriate boundary conditions:

$$\Psi_N|_{x=-d} = \Psi_B|_{x=-d}, \quad \Psi_B|_{x=0} = \Psi_S|_{x=0}. \quad (16)$$

These boundary conditions yield eight linear homogeneous equations for the coefficients r , r_A , t , t' , p , q , m , and n .

After some straightforward but cumbersome algebra, we find that

$$r = e^{-2ik_nd} \frac{\mathcal{N}}{\mathcal{D}}, \quad (17)$$

$$\begin{aligned} \mathcal{N} = & [e^{i\alpha} \cos(k_b d + \theta) - i \sin(k_b d)] \\ & - \rho [\cos(k_b d - \theta) - i e^{i\alpha} \sin(k_b d)], \end{aligned} \quad (18)$$

$$\begin{aligned} \mathcal{D} = & [e^{-i\alpha} \cos(k_b d + \theta) + i \sin(k_b d)] \\ & + \rho [\cos(k_b d - \theta) + i e^{-i\alpha} \sin(k_b d)], \end{aligned} \quad (19)$$

$$\begin{aligned} t' = & \frac{e^{-ik_nd}}{\cos(\theta)[\Gamma e^{-i\beta} + e^{i\beta}]} \left([\cos(k_b d - \theta) - i e^{i\alpha} \sin(k_b d)] \right. \\ & \left. + r e^{ik_nd} [\cos(k_b d - \theta) + i e^{-i\alpha} \sin(k_b d)] \right), \end{aligned} \quad (20)$$

$$t = \Gamma t', \quad (21)$$

$$r_A = \frac{t(\Gamma + 1)e^{ik'_n d} \cos(\theta') e^{-i\phi}}{\cos(k'_b d - \theta') - i e^{-i\alpha'} \sin(k'_b d)}, \quad (22)$$

where the parameters Γ and ρ can be expressed in terms of γ , β , θ , θ' , α , and α' (Eqs. 6, 9, 10, and 13) as

$$\rho = \frac{-\Gamma e^{i(\gamma-\beta)} + e^{-i(\gamma-\beta)}}{\Gamma e^{-i\beta} + e^{i\beta}}, \quad (23)$$

$$\Gamma = \frac{e^{-i\gamma} - \eta}{e^{i\gamma} + \eta}, \quad (24)$$

$$\eta = \frac{e^{-i\alpha'} \cos(k'_b d + \theta') - i \sin(k'_b d)}{\cos(k'_b d - \theta') - i e^{-i\alpha'} \sin(k'_b d)}. \quad (25)$$

The tunneling conductance of the NBS junction can now be expressed in terms of r and r_A by¹⁶

$$\frac{G(eV)}{G_0(eV)} = \int_0^{\alpha_c} \left(1 - |r|^2 + |r_A|^2 \frac{\cos(\alpha')}{\cos(\alpha)} \right) \cos(\alpha) d\alpha, \quad (26)$$

where $G_0 = 4e^2 N(eV)/h$ is the ballistic conductance of metallic graphene, eV denotes the bias voltage, and $N(\epsilon) = (E_F + \epsilon)w/(\pi \hbar v_F)$ denotes the number of available channels for

a graphene sample of width w . For $eV \ll E_F$, G_0 is a constant. Eq. 26 can be evaluated numerically to yield the tunneling conductance of the NBS junction for arbitrary parameter values. We note at the outset, that $G = 0$ when $\alpha_c = 0$. This occurs in two situations. First, when $eV = E_F$ and $V_0 \geq 2E_F$ so that $\alpha_c = \alpha_c^{(1)}$ vanishes. For this situation to arise, $E_F + U_0 > \Delta > E_F$ which means that U_0 has to be finite. Second, $\alpha_c = \alpha_c^{(2)} = 0$ when $eV = 0$ and $E_F = V_0$, so that the zero-bias conductance vanishes when the barrier potential matches the Fermi energy of the normal side⁶²

We now make contact with the results of the thin barrier limit. We note that since there are no condition on the derivatives of wavefunctions in graphene NBS junctions, the standard delta function potential approximation for thin barrier¹⁶ can not be taken the outset, but has to be taken at the end of the calculation. This limit is defined as $d/\lambda \rightarrow 0$ and $V_0/E_F \rightarrow \infty$ such that the dimensionless barrier strength

$$\chi = V_0 d / \hbar v_F = 2\pi \left(\frac{V_0}{E_F} \right) \left(\frac{d}{\lambda} \right) \quad (27)$$

remains finite. In this limit, as can be seen from Eqs. 6, 9 and 10, $\theta, \theta', k_n d, k'_n d \rightarrow 0$ and $k_b d, k'_b d \rightarrow \chi$ so that the expressions for Γ , ρ and η (Eq. 25)

$$\begin{aligned} \Gamma^{\text{tb}} &= \frac{e^{-i\gamma} - \eta^{\text{tb}}}{e^{i\gamma} + \eta^{\text{tb}}}, \quad \eta^{\text{tb}} = \frac{e^{-i\alpha'} \cos(\chi) - i \sin(\chi)}{\cos(\chi) - i e^{-i\alpha'} \sin(\chi)}, \\ \rho^{\text{tb}} &= \frac{e^{-i(\gamma-\beta)} - \Gamma^{\text{tb}} e^{i(\gamma-\beta)}}{\Gamma^{\text{tb}} e^{-i\beta} + e^{i\beta}}. \end{aligned} \quad (28)$$

where the superscript "tb" denotes thin barrier. Using the above-mentioned relations, we also obtain

$$\begin{aligned} r^{\text{tb}} &= \frac{\cos(\chi) (e^{i\alpha} - \rho^{\text{tb}}) - i \sin(\chi) (1 - \rho^{\text{tb}} e^{i\alpha})}{\cos(\chi) (e^{-i\alpha} + \rho^{\text{tb}}) + i \sin(\chi) (1 + \rho^{\text{tb}} e^{-i\alpha})}, \\ t'^{\text{tb}} &= \frac{\cos(\chi) (1 + r^{\text{tb}}) - i \sin(\chi) (e^{i\alpha} - r^{\text{tb}} e^{-i\alpha})}{\Gamma e^{-i\beta} + e^{i\beta}}, \\ t^{\text{tb}} &= \Gamma t'^{\text{tb}}, \\ r_A^{\text{tb}} &= \frac{t'^{\text{tb}} (\Gamma + 1) e^{-i\phi}}{\cos(\chi) - i e^{-i\alpha'} \sin(\chi)}. \end{aligned} \quad (29)$$

Eqs. 28 and 29 are precisely the result obtained in Ref. 17 for the tunneling conductance of a thin graphene NBS junction. The result obtained for a zero barrier in Ref. 11 can be now easily obtained from Eqs. 28 and 29 by substituting $\chi = 0$ in these equations.

1. Qualitative Discussions

In this section, we shall analyze the formulae for tunneling conductance obtained in above section. First we aim to obtain a qualitative understanding of the behavior of the tunneling conductance for finite barrier strength. To this end, we note from Eq. 26 that the maxima of the tunneling conductance must occur where $|r|^2$ is minimum. In fact, if $|r|^2 = 0$ for all transverse momenta, the tunneling conductance reaches its value $2G_0$. Therefore we shall first try to analyze the expression of r (Eq. 17) for subgap voltages and when the Fermi surfaces of the normal and superconducting sides are aligned with each other ($U_0 = 0$). In this case, we need $\Delta_0 \ll E_F$. So for subgap tunneling conductance, we have $\epsilon \leq \Delta_0 \ll E_F$. In this limit, $\alpha \simeq -\alpha' \simeq \gamma$ (Eqs. 6 and 10), $k_b \simeq k'_b$, and $\theta \simeq -\theta'$ (Eq. 9). Using these, one can write

$$\eta = \frac{e^{i\alpha} \cos(k_b d - \theta) - i \sin(k_b d)}{\cos(k_b d + \theta) - i e^{i\alpha} \sin(k_b d)}, \quad (30)$$

$$\rho = \frac{\eta \cos(\alpha - \beta) + i \sin(\beta)}{\cos(\alpha + \beta) + i \eta \sin(\beta)}. \quad (31)$$

Substituting Eq. 31 in the expression of \mathcal{N} , we find that the numerator of the reflection amplitude r becomes (Eqs. 17 and 18)

$$\begin{aligned} \mathcal{N} = \frac{e^{i\alpha}}{D_0} & \left[-4 \sin(\alpha) \sin(\beta) \cos(k_b d - \theta) \right. \\ & \times \left[-i \cos(\alpha) \sin(k_b d) \right. \\ & \left. + (\cos(k_b d - \theta) + \cos(k_b d + \theta))/2 \right] \\ & + 2 [\cos(k_b d + \theta) - \cos(k_b d - \theta)] \\ & \times \left[\cos(\alpha - \beta) \{ \cos(\alpha) + [\cos(k_b d - \theta) \right. \\ & \left. + \cos(k_b d + \theta)] / 2 \} + \sin(k_b d) \sin(\beta) \right] \Big], \end{aligned} \quad (32)$$

$$\begin{aligned} D_0 = & \cos(k_b d + \theta) \cos(\alpha + \beta) + \sin(k_b d) \sin(\beta) \\ & + i e^{i\alpha} [\cos(k_b d - \theta) \sin(\beta) - \sin(k_b d) \cos(\alpha + \beta)]. \end{aligned} \quad (33)$$

From the expression of \mathcal{N} (Eq. 32), we note the following features. First, for normal incidence ($\alpha = 0$) where $\theta = \theta' = 0$, \mathcal{N} and hence r (Eq. 17) vanishes. Thus the barrier is reflectionless for quasiparticles which incident normally on the barrier for arbitrary barrier

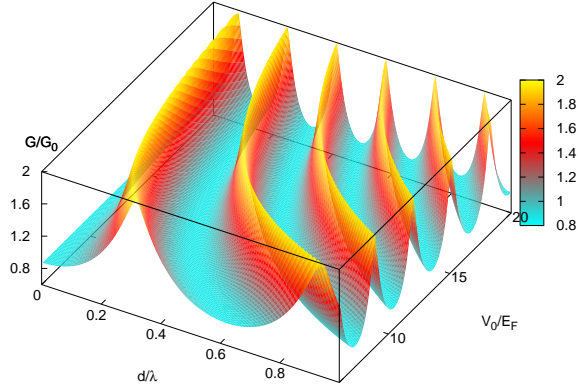


FIG. 3. Plot of zero-bias tunneling conductance for $U_0 = 0$ and $\Delta_0 = 0.01E_F$ as a function of gate voltage V_0 and barrier thickness d . Note that the oscillatory behavior of the tunneling conductance persists for the entire range of V_0 and d .

thickness d and strength of the applied voltage V_0 . This is a manifestation of Klein paradox for Dirac-Bogoliubov quasiparticles⁷. However, this feature is not manifested in tunneling conductance G (Eq. 26) which receives contribution from all angles of incidence. Second, apart from the above-mentioned cases, r never vanishes for all angles of incidence α and arbitrary $eV < \Delta_0$ unless $\theta = \theta'$. Thus the subgap tunneling conductance is not expected

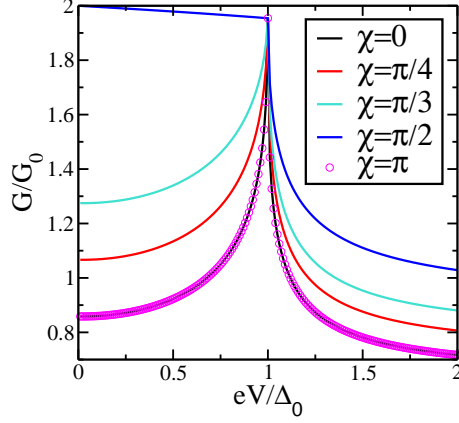


FIG. 4. Plot of tunneling conductance of a NBS junction graphene as a function of bias voltage for different effective barrier strengths for $U_0 = 0$ and $\Delta_0 = 0.01E_F$. Note that the curves for $\chi = 0$ (black line) and $\chi = \pi$ (pink circles) coincide reflecting π periodicity.

to reach a maximum value of $2G_0$ as long as the thin barrier limit is not satisfied. However, in practice, for barriers with $V_0 > 4E_F$, the difference between θ and θ' turns out to be small for all $q \leq k_F$ (≤ 0.25 for $q \leq k_F$ and $eV = 0$) so that the contribution to \mathcal{N} (Eq. 32) from the terms $\sim (\cos(k_b d + \theta) - \cos(k_b d - \theta))$ becomes negligible. Thus $|r|^2$ can become quite small for special values of V_0 for all $q \leq k_F$ so that the maximum value of tunneling conductance can reach close to $2G_0$. Third, for large V_0 , for which the contribution of terms $\sim (\cos(k_b d + \theta) - \cos(k_b d - \theta))$ becomes negligible, \mathcal{N} and hence r becomes very small when the applied voltage matches the gap edge *i.e.* $\sin(\beta) = 0$ (Eq. 32). Thus the tunneling conductance curves approaches close to its maximum value $2G_0$ and becomes independent of the gate voltage V_0 at the gap edge $eV = \Delta_0$ for $\Delta_0 \ll E_F$, as is also seen for conventional NBS junctions¹⁶. Fourth, in the thin barrier limit, ($V_0/E_F \rightarrow \infty$ and $d/\lambda \rightarrow 0$), $\theta \rightarrow 0$ and $k_b d \rightarrow \chi$, so that the contribution of the terms $\sim (\cos(k_b d + \theta) - \cos(k_b d - \theta))$ in Eq. 32 vanishes and one gets

$$\mathcal{N}^{tb} = \frac{2 \sin(\alpha) [\sin(\chi + \beta) - \sin(\chi - \beta)]}{D_0^{tb}} \times [-\cos(\chi) + i \sin(\chi) \cos(\alpha)], \quad (34)$$

$$D_0^{tb} = \cos(\chi) \cos(\alpha + \beta) + \sin(\chi) \sin(\beta) + i e^{i\alpha} \times [\cos(\chi) \sin(\beta) - \sin(\chi) \cos(\alpha + \beta)]. \quad (35)$$

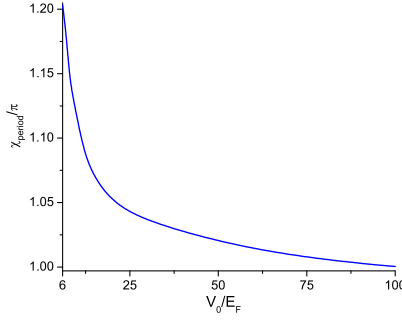


FIG. 5. Plot of periodicity χ_{period} of oscillations of tunneling conductance as a function of applied gate voltage V_0 for $U_0 = 0$ and $\Delta_0 = 0.01E_F$. Note that the periodicity approaches π as the voltage increases since the junction approaches the thin barrier limit.

\mathcal{N}^{tb} and hence r^{tb} (Eq. 29) vanishes at $\chi = (n + 1/2)\pi$ which yields the transmission resonance condition for NBS junctions in graphene and is given in Fig.4¹⁷.

Fifth, as can be seen from Eqs. 17 and 22, both $|r|^2$ and $|r_A|^2$ are periodic functions of V_0 and d since both k_b and θ depend on V_0 . Thus the oscillatory behavior of subgap tunneling conductance as a function of applied gate voltage V_0 or barrier thickness d is a general feature of graphene NBS junctions with $d \ll \xi$. However, unlike the thin barrier limit, for an arbitrary NBS junction, $k_b d = \chi \sqrt{(E_F/V_0 - 1)^2 + \hbar^2 v_F^2 q^2 / V_0^2} \neq \chi$, and $\theta \neq 0$. Thus the period of oscillations of $|r|^2$ and $|r_A|^2$ will depend on V_0 and should deviate from their universal value π in the thin barrier limits¹⁷. Finally, we note from Eqs. 17, 26 and 34 that in the thin barrier limit (and therefore for large V_0), the amplitude of oscillations of the zero-bias conductance for a fixed V_0 , defined as $[G_{\text{max}}(eV = 0; V_0) - G_{\text{min}}(eV = 0; V_0)]/G_0$, which depends on the difference of $|r(\chi = (n + 1/2)\pi)|^2$ and $|r(\chi = n\pi)|^2$ becomes independent of χ or the applied gate voltage V_0 .

2. Numerical Results

The above-mentioned discussion is corroborated by numerical evaluation of the tunneling conductance as shown in Figs. 3, 5, 6 and 7. From Fig. 3, which plots zero-bias tunneling conductance $G(eV = 0)$ as a function of V_0 and d , we find that $G(eV = 0)$ is an oscillatory function of both V_0 and d and reaches close to its maximum value of $2G_0$ throughout the plotted range of V_0 and d . Further, as seen from Fig. 5, the periodicity of these oscillations

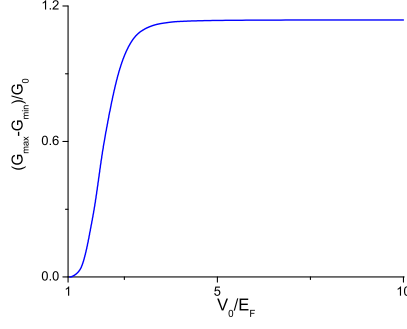


FIG. 6. Plot of the amplitude $[G_{\max}(eV = 0; V_0) - G_{\min}(eV = 0; V_0)]/G_0 \equiv (G_{\max} - G_{\min})/G_0$ of zero-bias tunneling conductance as a function of the applied gate voltage V_0 for $U_0 = 0$ and $\Delta_0 = 0.01E_F$. Note that G reaches $2G_0$ for $V_0 \geq 4E_F$ where the amplitude become independent of the applied gate voltage as in the thin barrier limit and vanishes for $V_0/E_F = 1$ as discussed in the text.

becomes a function of V_0 . To measure the periodicity of these oscillations, the tunneling conductance is plotted for a fixed V_0 as a function of d . The periodicity of the conductance d_{period} is noted down from these plots and $\chi_{\text{period}} = V_0 d_{\text{period}}/\hbar v_F$ is computed. Fig. 5 clearly shows that χ_{period} deviate significantly from their thin barrier value π for low enough V_0 and diverges at $V_0 \rightarrow E_F$ ⁶³. Fig. 6 shows the amplitude of oscillations of zero-bias conductance as a function of V_0 . We note that maximum of the zero-bias tunneling conductance $G_{\max}(eV = 0)$ reaches close to $2G_0$ for $V_0 \geq V_{0c} \simeq 4E_F$. For $V \geq V_{0c}$, the amplitude becomes independent of the applied voltage as in the thin barrier limit, as shown in Fig. 6. For $V_0 \rightarrow E_F$, $\alpha_c = \alpha_c^{(2)} \rightarrow 0$, so that $G(eV = 0) \rightarrow 0$ and hence the amplitude vanishes. Finally, in Fig. 7, we plot the tunneling conductance G as a function of the applied bias-voltage eV and applied gate voltage V_0 for $d = 0.4\lambda$. We find that, as expected from Eq. 34, G reaches close to $2G_0$ at the gap edge for all $V_0 \geq 6E_F$. Also, as in the thin barrier limit, the oscillation amplitudes for the subgap tunneling conductance is maximum at zero-bias and shrinks to zero at the gap edge $eV = \Delta_0$, where the tunneling conductance become independent of the gate voltage.

Next, we consider the case $U_0 \neq 0$, so that $\Delta_0 \simeq E_F \ll (E_F + U_0)$. In this regime, there is a large mismatch of Fermi surfaces on the normal and superconducting sides. Such a mismatch is well-known to act as an effective barrier for NBS junctions. Consequently,

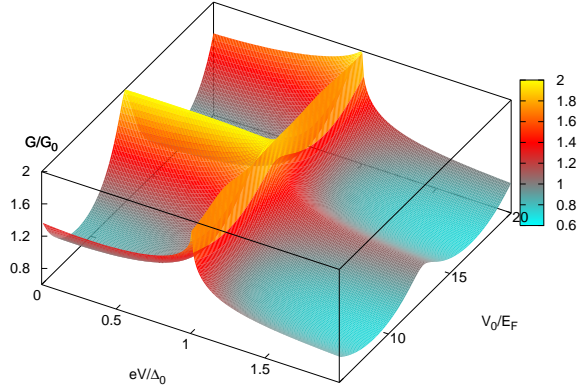


FIG. 7. Plot of tunneling conductance as a function of the bias-voltage eV and gate voltage V_0 for $d = 0.4\lambda$ and $\Delta_0 = 0.01E_F$. Note that for large V_0 , the tunneling conductance at $eV = \Delta_0$ is close to $2G_0$ and becomes independent of V_0 (see text for discussion).

additional barrier created by the gate voltage becomes irrelevant, and we expect the tunneling conductance to become independent of the applied gate voltage V_0 . Also note that at $eV = E_F$, $\alpha_c = 0$ (Eq. 14). Hence there is no Andreev reflection and consequently G_0 vanishes for all values of the applied gate voltage for this bias voltage. Our results in this limit, coincides with those of Ref. 11. Finally in Fig. 9, we show the dependence of amplitude of

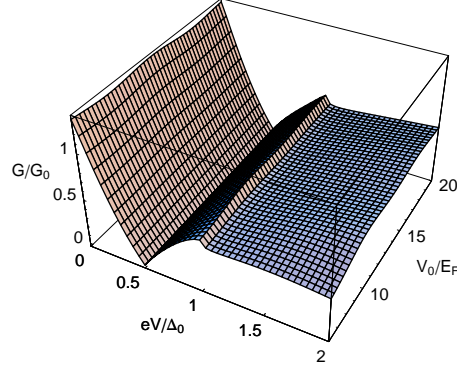


FIG. 8. Plot of tunneling conductance as a function of the bias-voltage eV and the gate voltage V_0 for $d = 0.4\lambda$, $\Delta_0 = 2E_F$ and $U_0 = 25E_F$. As discussed in the text, the tunneling conductance is virtually independent of the applied gate voltage V_0 due to the presence of a large U_0 . Note that maximum angle of incidence for which Andreev reflection can take place vanishes at $eV = E_F$ leading to vanishing of G at this bias voltage.

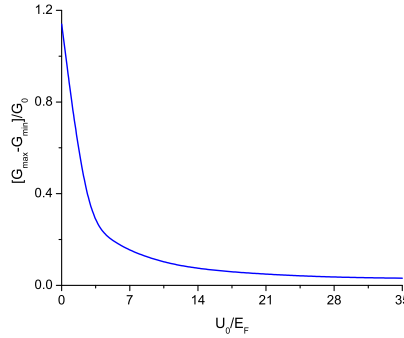


FIG. 9. Plot of amplitude of oscillation $(G_{\max} - G_{\min})/G_0$ of zero-bias tunneling conductance as a function of U_0/E_F for $V_0 = 6E_F$ and $\Delta_0 = 0.01E_F$. The oscillation amplitudes always decay monotonically with increasing U_0 independent of V_0 .

oscillation of zero-bias tunneling conductance on U_0 for the applied bias voltages $V_0 = 6E_F$ and $\Delta_0 = 0.01E_F$. As expected, the oscillation amplitude with decreases monotonically with increasing U_0 . We have verified that this feature is independent of the applied gate voltage V_0 as long as $V_0 \geq V_{0c}$.

B. SBS junction

For this junction, the region **I** in Fig 1 is a superconducting region and the pair-potential can be given as

$$\Delta(\mathbf{r}) = \Delta_0 [\exp(i\phi_2)\theta(x) + \exp(i\phi_1)\theta(x+d)] \quad (36)$$

where Δ_0 is the amplitude and $\phi_{1(2)}$ are the phases of the induced superconducting order parameters in regions I (II) as shown in Fig.1, and θ is the Heaviside step function. Solving Eq. 2, the wavefunctions in the superconducting and the barriers regions are obtained. In region I, the wavefunctions for the DBdG quasiparticles moving along $\pm x$ direction with a transverse momentum $k_y = q = 2\pi n/L$ (for integer n) and energy ϵ , are given by¹¹

$$\psi_I^\pm = (u_1^\pm, u_2^\pm, u_3^\pm, u_4^\pm) e^{[i(\pm k_s x + qy) + \kappa x]} \quad (37)$$

where

$$\begin{aligned} \frac{u_2^\pm}{u_1^\pm} &= \pm \exp(\pm i\gamma), & \frac{u_3^\pm}{u_1^\pm} &= \exp[-i(\phi_1 \mp \beta)], \\ \frac{u_4^\pm}{u_1^\pm} &= \pm \exp[\pm i(\mp \phi_1 + \beta + \gamma)], \end{aligned} \quad (38)$$

and $\sum_{i=1,4} |u_i|^2 \simeq 2\kappa$ is the normalization condition for the wavefunction for $d \ll \kappa^{-1}$, where $\kappa^{-1} = (\hbar v_F)^2 k_s / [E_F \Delta_0 \sin(\beta)]$ is the localization length. Here $k_s = \sqrt{(E_F/\hbar v_F)^2 - q^2}$, γ , the angle of incidence for the quasiparticles, is given by $\sin(\gamma) = \hbar v_F q / E_F$, and β is given by

$$\begin{aligned} \beta &= \cos^{-1}(\epsilon/\Delta_0) \quad \text{if } |\epsilon| < \Delta_0, \\ &= -i \cosh^{-1}(\epsilon/\Delta_0) \quad \text{if } |\epsilon| > \Delta_0, \end{aligned} \quad (39)$$

Note that for $|\epsilon| > \Delta_0$, κ becomes imaginary and the quasiparticles can propagate in the bulk of the superconductor. The wavefunctions in region II ($x \geq 0$) can also be obtained in a similar manner

$$\psi_{II}^\pm = (v_1^\pm, v_2^\pm, v_3^\pm, v_4^\pm) e^{[i(\pm k_s x + qy) - \kappa x]}, \quad (40)$$

where $\sum_{i=1,4} |v_i|^2 = 2\kappa$ and the coefficients v_i are given by

$$\begin{aligned} \frac{v_2^\pm}{v_1^\pm} &= \pm \exp(\pm i\gamma), & \frac{v_3^\pm}{v_1^\pm} &= \exp[-i(\phi_2 \pm \beta)], \\ \frac{v_4^\pm}{v_1^\pm} &= \pm \exp[\pm i(\mp \phi_2 - \beta + \gamma)], \end{aligned} \quad (41)$$

The wavefunctions for electrons and holes moving along $\pm x$ in the barrier region is given by

$$\begin{aligned}\psi_B^{e\pm} &= (1, \pm e^{\pm i\theta}, 0, 0) \exp [i (\pm k_b x + qy)] / \sqrt{2d}, \\ \psi_B^{h\pm} &= (0, 0, 1, \pm e^{\mp i\theta'}) \exp [i (\pm k'_b x + qy)] / \sqrt{2d}.\end{aligned}$$

Here the angle of incidence of the electron(hole) $\theta(\theta')$ and is given by:

$$\begin{aligned}\sin [\theta(\theta')] &= \frac{\hbar v_F q}{\epsilon + (-)(E_F - V_0)} \\ k_b(k'_b) &= \sqrt{\left(\frac{\epsilon + (-)(E_F - V_0)}{\hbar v_F} \right)^2 - q^2}\end{aligned}\tag{42}$$

To compute the Josephson current in the SBS junction, the energy dispersion of the subgap Andreev bound states are found which are localized with localization length κ^{-1} at the barrier^{43,44}. The energy dispersion ϵ_n (corresponding to the subgap state characterized by the quantum number n) of these states depends on the phase difference $\phi = \phi_2 - \phi_1$ between the superconductors. The Josephson current I across the junction at a temperature T_0 is given by^{13,43}

$$I(\phi; \chi, T_0) = \frac{4e}{\hbar} \sum_n \sum_{q=-k_F}^{k_F} \frac{\partial \epsilon_n}{\partial \phi} f(\epsilon_n),\tag{43}$$

where $f(x) = 1/(e^{x/(k_B T_0)} + 1)$ is the Fermi distribution function and k_B is the Boltzman constant⁶⁴

To obtain these subgap Andreev bound states, boundary conditions at the barrier are imposed. The wavefunctions in the superconducting and barrier regions are constructed using Eqs. 37, 40 and 42 as

$$\begin{aligned}\Psi_I &= a_1 \psi_I^+ + b_1 \psi_I^- \quad \Psi_{II} = a_2 \psi_{II}^+ + b_2 \psi_{II}^-, \\ \Psi_B &= p \psi_B^{e+} + q \psi_B^{e-} + r \psi_B^{h+} + s \psi_B^{h-},\end{aligned}\tag{44}$$

where $a_1(a_2)$ and $b_1(b_2)$ are the amplitudes of right and left moving DBdG quasiparticles in region I(II) and $p(q)$ and $r(s)$ are the amplitudes of right(left) moving electron and holes respectively in the barrier. These wavefunctions satisfy the boundary conditions:

$$\Psi_I|_{x=-d} = \Psi_B|_{x=-d}, \quad \Psi_B|_{x=0} = \Psi_{II}|_{x=0}.\tag{45}$$

Substituting Eqs. 37, 40, 42, and 44 in Eq. 45, we get eight linear homogeneous equations for the coefficients $a_{i=1,2}$, $b_{i=1,2}$, p , q , r , and s , so that the condition for non-zero solutions of these coefficients can be obtained as

$$\mathcal{A}' \sin(2\beta) + \mathcal{B}' \cos(2\beta) + \mathcal{C}' = 0 \quad (46)$$

where \mathcal{A}' , \mathcal{B}' , and \mathcal{C}' are given by

$$\begin{aligned} \mathcal{A}' &= \cos(k'_b d) \cos(\gamma) \cos(\theta') \sin(k_b d) (\sin(\gamma) \sin(\theta) - 1) \\ &\quad + \cos(k_b d) \cos(\gamma) \cos(\theta) \sin(k'_b d) \\ &\quad + \frac{1}{2} \cos(k_b d) \cos(\theta) \sin(2\gamma) \sin(\theta') \sin(k'_b d) \\ \mathcal{B}' &= \sin(k'_b d) \sin(k_b d) [-1 + \sin(\theta) \sin(\gamma) \\ &\quad - \sin(\theta') \sin(\gamma) + \sin(\theta) \sin(\theta') \sin^2(\gamma)] \\ &\quad - \cos(k_b d) \cos(k'_b d) \cos^2(\gamma) \cos(\theta) \cos(\theta') \\ \mathcal{C}' &= \cos^2(\gamma) \cos(\theta) \cos(\theta') \cos(\phi) - \sin(k_b d) \sin(k'_b d) \\ &\quad \times [\sin(\theta) \sin(\theta') - \sin^2(\gamma) \\ &\quad + \sin(\gamma) (\sin(\theta) - \sin(\theta'))] \end{aligned} \quad (47)$$

Note that in general the coefficients \mathcal{A}' , \mathcal{B}' , and \mathcal{C}' depends on ϵ through k_b , k'_b , θ and θ' which makes it impossible to find an analytical solution for Eq. 46. However, for subgap states in graphene SBS junctions, $\epsilon \leq \Delta_0 \ll E_F$. Further, for short tunnel barrier we have $|V_0 - E_F| \geq E_F$. In this regime, as can be seen from Eqs. 42, \mathcal{A}' , \mathcal{B}' , and \mathcal{C}' become independent of ϵ since $k_b \simeq k'_b \simeq k_1 = \sqrt{[(E_F - V_0)/\hbar v_F]^2 - q^2}$ and $\theta \simeq -\theta' \simeq \theta_1 = \sin^{-1} [\hbar v_F q / (E_F - V_0)]$ so that the ϵ dependence of k_b , k'_b , θ and θ' can be neglected. In this regime one finds that $\mathcal{A}', \mathcal{B}', \mathcal{C}' \rightarrow \mathcal{A}, \mathcal{B}, \mathcal{C}$ where

$$\begin{aligned} \mathcal{A} &= 0 \\ \mathcal{B} &= -\sin^2(k_1 d) [1 - \sin(\gamma) \sin(\theta_1)]^2 \\ &\quad - \cos^2(k_1 d) \cos^2(\gamma) \cos^2(\theta_1) \\ \mathcal{C} &= \sin^2(k_1 d) [\sin(\gamma) - \sin(\theta_1)]^2 \\ &\quad + \cos^2(\gamma) \cos^2(\theta_1) \cos(\phi) \end{aligned} \quad (48)$$

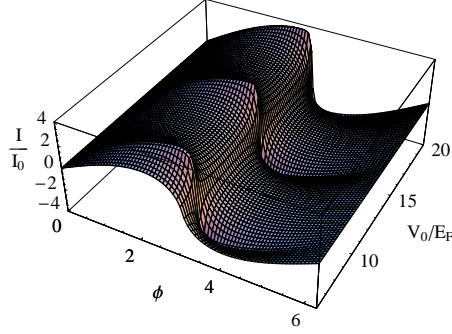


FIG. 10. Plot of Josephson current I as a function of phase difference ϕ and the applied gate voltage V_0 for $k_B T_0 = 0.01\Delta_0$ and $d = 0.5\lambda$ showing oscillatory behavior of I/I_0 as a function of the applied gate voltage.

The dispersion of the Andreev subgap states can now be obtained from Eqs. 46 and 39. There are two Andreev subgap states with energies $\epsilon_{\pm} = \pm\epsilon$ where

$$\epsilon = \Delta_0 \sqrt{1/2 - \mathcal{C}/2\mathcal{B}} \quad (49)$$

Using Eq. 43, one can now obtain the expression for the Josephson current

$$\begin{aligned} I(\phi, V_0, d, T_0) &= I_0 g(\phi, V_0, d, T_0), \\ g(\phi, V_0, d, T_0) &= \int_{-\pi/2}^{\pi/2} d\gamma \left[\frac{\cos^3(\gamma) \cos^2(\theta_1) \sin(\phi)}{\mathcal{B}\epsilon/\Delta_0} \right. \\ &\quad \left. \times \tanh(\epsilon/2k_B T_0) \right] \end{aligned} \quad (50)$$

where $I_0 = e\Delta_0 E_F L / 2\hbar^2 \pi v_F$ and we have replaced $\sum_q \rightarrow E_F L / (2\pi\hbar v_F) \int_{-\pi/2}^{\pi/2} d\gamma \cos(\gamma)$ as appropriate for wide junctions¹³.

The dispersion of the Andreev subgap states and the Josephson current in graphene SBS junctions, in complete contrast to their conventional counterparts^{20,21,43}, is found to be an oscillatory function of the applied gate voltage V_0 and the barrier thickness d . This statement can be most easily checked by plotting the Josephson current I as a function of the phase difference ϕ and the applied gate voltage V_0 for a representative barrier thickness $d = 0.5\lambda$ and temperature $k_B T_0 = 0.01\Delta_0$, as done in Fig. 10. In Fig. 11, we plot the critical current of these junctions $I_c(V_0, d, T_0) = \text{Max}[I(\phi, V_0, d, T_0)]$ as a function of the applied gate voltage V_0 and barrier thickness d for low temperature $k_B T_0 = 0.01\Delta_0$. The critical current of these

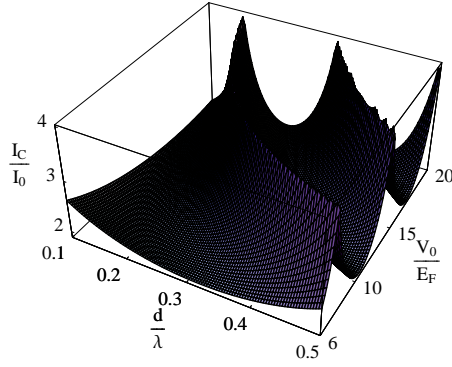


FIG. 11. Plot of I_c/I_0 vs the applied gate voltage V_0 and the junction thickness d for $T_0 = 0.01\Delta_0$.

graphene SBS junctions is an oscillatory function of both V_0 and d . This behavior is to be contrasted with those of conventional junctions where the critical current is a monotonically decreasing function of both applied bias voltage V_0 and junction thickness d ^{20,21,43}.

We analyze a few other properties of these oscillations. To find the amplitude of oscillation, we compute I_c as a function of V_0 (for a representative value of $d = 0.3\lambda$), note the maximum (I_c^{\max}) and minimum (I_c^{\min}) values of I_c , and calculate the amplitude $I_c^{\max} - I_c^{\min}$. The procedure is repeated for several temperatures T_0 and the result is plotted in Fig. 12 which shows that the amplitude of oscillations decreases monotonically as a function of temperature. Next, we discuss the period of oscillation of the critical current. To obtain the period, the critical current I_c as a function of barrier width d for the fixed applied gate voltage V_0 is computed and d_{period} is noted down. Then $\chi_{\text{period}} = V_0 d_{\text{period}} / \hbar v_F$ is computed and χ_{period} as a function of V_0 for $k_B T_0 = 0.01\Delta_0$ is plotted as shown in Fig. 13. It is found that χ_{period} decreases with V_0 and approaches an universal value π for large $V_0 \geq 20E_F$. This property, as we shall see in the next section, can be understood by analysis of graphene SBS junctions in the thin barrier limit ($V_0 \rightarrow \infty$ and $d \rightarrow 0$ such that $\chi = V_0 d / \hbar v_F$ remains finite¹⁷) and is a direct consequence of transmission resonance phenomenon of DBdG quasiparticles in superconducting graphene.

1. Thin barrier limit

In the limit of thin barrier, where $V_0 \rightarrow \infty$ and $d \rightarrow 0$ such that $\chi = V_0 d / \hbar v_F$ remains finite, $\theta_1 \rightarrow 0$ and $k_1 d \rightarrow \chi$. From Eqs. 48 and 49, we find that in this limit, the dispersion

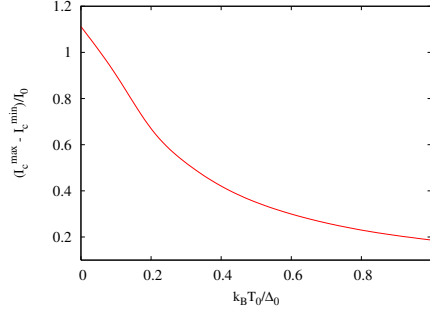


FIG. 12. Plot of the temperature dependence of the amplitude of oscillations of I_c (given by $[I_c^{\max}(d) - I_c^{\min}(d)]/I_0$) for $d = 0.3\lambda$. The amplitude is measured by noting the maximum and minimum values of the critical current by varying V_0 for a fixed d .

of the Andreev bound states becomes

$$\epsilon_{\pm}^{\text{tb}}(q, \phi; \chi) = \pm \Delta_0 \sqrt{1 - T(\gamma, \chi) \sin^2(\phi/2)}, \quad (51)$$

$$T(\gamma, \chi) = \frac{\cos^2(\gamma)}{1 - \cos^2(\chi) \sin^2(\gamma)}. \quad (52)$$

where the superscript ‘tb’ denote thin barrier limit. The Josephson current I can be obtained substituting Eq. 52 in Eq. 43. In the limit of wide junctions, one gets

$$\begin{aligned} I^{\text{tb}}(\phi, \chi, T_0) &= I_0 g^{\text{tb}}(\phi, \chi, T_0), \\ g^{\text{tb}}(\phi, \chi, T_0) &= \int_{-\pi/2}^{\pi/2} d\gamma \left[\frac{T(\gamma, \chi) \cos(\gamma) \text{Aschemat} \sin(\phi)}{\sqrt{1 - T(\gamma, \chi) \sin^2(\phi/2)}} \right. \\ &\quad \left. \times \tanh(\epsilon_+/2k_B T_0) \right]. \end{aligned} \quad (53)$$

We find that the Josephson current in graphene SBS junctions is a π periodic oscillatory function of the effective barrier strength χ in the thin barrier limit. Further we observe that the transmission probability of the DBdG quasiparticles in a thin SBS junction is given by $T(\gamma, \chi)$ which is also the transmission probability of a Dirac quasiparticle through a square potential barrier as noted in Ref. 6. Note that the transmission becomes unity for normal incidence ($\gamma = 0$) and when $\chi = n\pi$. The former condition is a manifestation of the Klein paradox for DBdG quasiparticles⁶. However, this property is not reflected in the Josephson current which receives contribution from quasiparticles approaching the

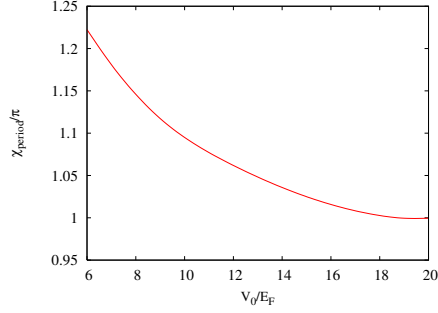


FIG. 13. Plot of χ_{period} of the critical current I_c as a function of V_0 . Note that χ_{period} approaches π as we approach the thin barrier limit.

junction at all angles of incidence. The latter condition ($\chi = n\pi$) represents transmission resonance condition of the DBdG quasiparticles. Thus the barrier becomes completely transparent to the approaching quasiparticles when $\chi = n\pi$ and in this limit the Josephson current reduces to its value for conventional tunnel junctions in the Kulik-Omelyanchuk limit: $I_c^{\text{tb}}(\phi, n\pi, T_0) = 4I_0 \sin(\phi/2) \text{Sgn}(\cos(\phi/2)) \tanh(\Delta_0 |\cos(\phi/2)| / 2k_B T_0)^{22}$. This yields the critical Josephson current $I_c^{\text{tb}}(\chi = n\pi) = 4I_0$ for $k_B T_0 \ll \Delta_0$. Note, however, that in contrast to conventional junctions $T(\gamma, \chi)$ can not be made arbitrarily small for all γ by increasing χ . Hence I_c^{tb} never reaches the Ambegaokar-Baratoff limit of conventional tunnel junctions²³. Instead, $I_c^{\text{tb}}(\chi)$ becomes a π periodic oscillatory function of χ . The amplitude of these oscillations decreases monotonically with temperature.

Finally, the product $I_c^{\text{tb}} R_N$ which is routinely used to characterize Josephson junctions^{20,21} is computed, where R_N is the normal state resistance of the junction. For graphene SBS junctions R_N corresponds to the resistance of a Dirac quasiparticle as it moves across a normal metal-barrier-normal metal junction. For short and wide junctions discussed here, it is given by $R_N = R_0 / s_1(\chi)$ where $R_0 = \pi^2 v_F \hbar^2 / (e^2 E_F L)$ and $s_1(\chi)$ is given by^{6,13}

$$s_1(\chi) = \int_{-\pi/2}^{\pi/2} d\gamma T(\gamma, \chi) \cdot \cos(\gamma). \quad (54)$$

Note that $s_1(\chi)$ and hence R_N is an oscillatory function of χ with minimum $0.5R_0$ at $\chi = n\pi$ and maximum $0.75R_0$ at $\chi = (n + 1/2)\pi$. The product $I_c^{\text{tb}} R_N$, for thin SBS junctions is given by

$$I_c^{\text{tb}} R_N = (\pi \Delta_0 / 2e) g_{\text{max}}^{\text{tb}}(\chi, T) / s_1(\chi), \quad (55)$$

where $g_{\text{max}}^{\text{tb}}(\chi)$ is the maximum value of $g^{\text{tb}}(\phi, \chi)$. Note that $I_c^{\text{tb}} R_N$ is independent of E_F and

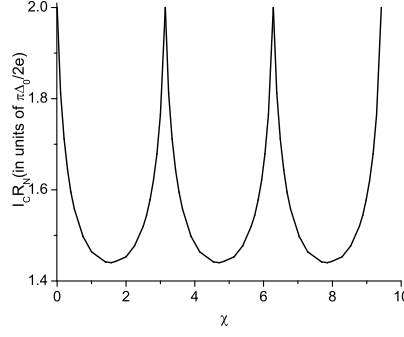


FIG. 14. Plot of $I_c^{\text{tb}} R_N$ as a function of χ . $I_c^{\text{tb}} R_N$ is an oscillatory bounded function of χ and never reaches its value $(\pi\Delta_0/2e)$ for conventional junctions in the Ambegaokar-Baratoff limit.

hence survives in the limit $E_F \rightarrow 0^{13}$. For $k_B T_0 \ll \Delta_0$, $g_{\text{max}}^{\text{tb}}(n\pi) = 4$ and $s_1(n\pi) = 2$, so that $I_c^{\text{tb}} R_N|_{\chi=n\pi} = \pi\Delta_0/e$ which coincides with Kulik-Omelyanchuk limit for conventional tunnel junctions^{22,44}. However, in contrast to the conventional junction, $I_c^{\text{tb}} R_N$ for graphene SBS junctions do not monotonically decrease to the Ambegaokar-Baratoff limit^{23,44} of $\pi\Delta_0/2e \simeq 1.57\Delta_0/e$ as χ is increased, but demonstrates π periodic oscillatory behavior and remains bounded between the values $\pi\Delta_0/e$ at $\chi = n\pi$ and $2.27\Delta_0/e$ at $\chi = (n + 1/2)\pi$, as shown in Fig. 14.

III. EXPERIMENTS

Superconductivity has recently been experimentally realized in graphene⁴². In the proposed experiment to observe the oscillatory behavior in the tunneling conductance and Josephson current, one needs to realize these junctions in graphene. The local barrier can be fabricated using methods of Refs. [5,41]. The easiest experimentally achievable regime corresponds to $\Delta_0 \ll E_F$ with aligned Fermi surfaces for the normal and superconducting regions. We suggest measurement of tunneling conductance curves at zero-bias ($eV = 0$) in this regime. Our prediction is that the zero-bias conductance will show an oscillatory behavior with the bias voltage. In graphene, typical Fermi energy can be $E_F \leq 40\text{meV}$ and the Fermi-wavelength is $\lambda \geq 100\text{nm}$ ^{5,6,41,42}. Effective barrier strengths of $\leq 80\text{meV}$ ⁶ and barrier widths of $d \simeq 10 - 50 \text{ nm}$ therefore specifies the range of experimentally feasible junctions^{5,6,41}. Consequently for experimental junctions, the ratio V_0/E_F can be arbitrarily

large within these parameter ranges by fixing V_0 and lowering E_F . Experimentally, one can set $5 \leq E_F \leq 20\text{meV}$ so that the conditions $\Delta_0 \ll E_F$ $V_0/E_F \gg 1$ is easily satisfied for realistic $\Delta_0 \sim 0.5\text{meV}$ and $V_0 = 200\text{meV}$. This sets the approximate range $V_0/E_F \geq 10$ for the experiments. Note that since the period (amplitude) of oscillations increases (decreases) as $V_0/E_F \rightarrow 1$, it is preferable to have sufficiently large values of V_0/E_F for experimental detection of these oscillations.

To check the oscillatory behavior of the zero-bias tunneling conductance, it would be necessary to change V_0 in small steps δV_0 . For barriers of a fixed width, for example with values of $d/\lambda = 0.3$, it will be enough to change V_0 in steps of approximately $20 - 30\text{meV}$, which should be experimentally feasible.

We note that for the above-mentioned range of V_0/E_F , the experimental junctions shall not always be in the thin barrier limit. For example, as is clear from Fig. 5, the periodicity of oscillations χ_{period} of the zero-bias tunneling conductance of such junctions shall be a function of V_0 and shall differ from π . This justifies the theoretical study of NBS junctions in graphene which are away from the thin barrier limit.

Apart from the above-mentioned experiments, it should also be possible to measure the tunneling conductance as a function of the applied bias voltage eV/Δ_0 for different applied gate voltages V_0 . Such measurements can be directly compared with Fig. 6. Finally, it might be also possible to create a relative bias U_0 between the Fermi surfaces in the normal and superconducting side and compare the dependence of oscillation amplitudes of zero-bias tunneling conductance on U_0 with the theoretical result shown in Fig. 8.

We also suggest measuring DC Josephson current in these junctions as a function of the applied voltage V_0 . Such experiments for conventional Josephson junctions are well-known⁴⁵. Further SNS junctions in graphene has also been recently been experimentally created^{42,46}. To observe the oscillatory behavior of the Josephson current, alike the procedure to measure the tunneling conductance, it would be necessary to change V_0 in small steps δV_0 . For barriers with fixed $d/\lambda = 0.3$ and $V_0/E_F = 10$, this would require changing V_0 in steps of approximately 30meV which is experimentally feasible. The Joule heating in such junctions, proportional to $I_c^2 R_N$, should also show measurable oscillatory behavior as a function of V_0 .

IV. KONDO EFFECT AND STM SPECTRA

A. Kondo effect in Graphene

In this section, we shall present a large N analysis for a generic local moment coupled to Dirac electrons in graphene to show that Kondo effect in graphene is unconventional can be tuned by gate voltage. We demonstrate the presence of a finite critical Kondo coupling strength in neutral graphene. We point out that local moments in graphene can lead to non Fermi-liquid ground state via multi channel Kondo effect.

The crucial requirement for occurrence of Kondo effect is that the embedded impurities should retain their magnetic moment in the presence of conduction of electrons of graphene. We will not quantitatively address the problem of local moment formation in the presence of Dirac sea of electrons in graphene in the present paper. We expect that large band width and small linearly vanishing density of states at the fermi level in graphene should make survival of impurity magnetic moment easier than in the conventional 3D metallic matrix. A qualitative estimate of the resultant Kondo coupling can be easily made considering hybridization of electrons in π band in graphene with d orbitals of transition metals. Typical hopping matrix elements for electrons in π band is $t \sim 2\text{eV}$ and effective Hubbard U in transition metals is 8eV . So the Kondo exchange $J \sim 4t^2/U$, estimated via standard Schrieffer-Wolf transformation, can be as large as 2 eV which is close to one of the largest $J \simeq 2.5\text{ eV}$ for Mn in Zn. Therefore it is customary to use Kondo Hamiltonian²⁴ to study the effect in Graphene.

1. Large N analysis

Our analysis begins with the Hamiltonian for non-interacting Dirac electron in graphene. In the presence of a gate voltage V , the Hamiltonian can be expressed in terms of electron annihilation operators $\Psi_{A(B)\alpha}^s$ at sublattice $A(B)$ and Dirac point $s = K, K'$ with spin $\alpha = \uparrow, \downarrow$ as

$$H = \int \frac{d^2k}{(2\pi)^2} \left(\Psi_{A\alpha}^{s\dagger}(\mathbf{k}), \Psi_{B\alpha}^{s\dagger}(\mathbf{k}) \right) \times \begin{pmatrix} eV & \hbar v_F(k_x - i \text{sgn}(s)k_y) \\ \hbar v_F(k_x + i \text{sgn}(s)k_y) & eV \end{pmatrix} \begin{pmatrix} \Psi_{A\alpha}^s(\mathbf{k}) \\ \Psi_{B\alpha}^s(\mathbf{k}) \end{pmatrix} \quad (56)$$

where $\text{sgn}(s) = 1(-1)$ for $s = K(K')$, v_F is the Fermi velocity of graphene, and all repeated indices are summed over. In Eq. 56 and rest of the analysis, we shall use an upper momentum cutoff $k_c = \Lambda/(\hbar v_F)$, where $\Lambda \simeq 2\text{eV}$ corresponds to energy up to which the linear Dirac dispersion is valid, for all momenta integrals.

Eq. 56 can be easily diagonalized to obtain the eigenvalues and eigenfunctions of the Dirac electrons: $E_{\pm} = eV \pm \hbar v_F k$ where $\mathbf{k} = (k_x, k_y) = (k, \theta)$ denote momenta in graphene and $(u_A^{\pm}, u_B^{\pm}) = 1/\sqrt{2}(1, \pm \exp(i\text{sgn}(s)\theta))$. Following Ref. 27, we now introduce the ξ fields, which represents low energy excitations with energies E_{\pm} , and write

$$\begin{aligned}\Psi_{A\alpha}^s(\mathbf{k}) &= \sum_{j=\pm} u_A^{sj} \xi_{j\alpha}^s = 1/\sqrt{2}(\xi_{+\alpha}^s(\mathbf{k}) + \xi_{-\alpha}^s(\mathbf{k})), \\ \Psi_{B\alpha}^s(\mathbf{k}) &= \exp(i\theta)/\sqrt{2}(\xi_{+\alpha}^s(\mathbf{k}) - \xi_{-\alpha}^s(\mathbf{k})).\end{aligned}\quad (57)$$

In what follows, we shall consider a single impurity to be centered around $\mathbf{x} = 0$. Thus to obtain an expression for the coupling term between the local moment and the conduction electrons, we shall need to obtain an expression for $\Psi(\mathbf{x} = 0) \equiv \Psi(0)$. To this end, we expand the ξ fields in angular momentum channels $\xi_{+\alpha}^s(\mathbf{k}) = \sum_{m=-\infty}^{\infty} e^{im\theta} \xi_{+\alpha}^{ms}(k)$, where we have written $\mathbf{k} = (k, \theta)$. After some straightforward algebra, one obtains

$$\begin{aligned}\Psi_{B\alpha}^s(0) &= \frac{1}{\sqrt{2}} \int_0^{k_c} \frac{k dk}{2\pi} \left(\xi_{+\alpha}^{-\text{sgn}(s)s}(k) - \xi_{-\alpha}^{-\text{sgn}(s)s}(k) \right), \\ \Psi_{A\alpha}^s(0) &= \frac{1}{\sqrt{2}} \int_0^{k_c} \frac{k dk}{2\pi} \left(\xi_{+\alpha}^{0s}(k) + \xi_{-\alpha}^{0s}(k) \right).\end{aligned}\quad (58)$$

Note that $\Psi_B(0)$ receives contribution from $m = \pm 1$ channel while for $\Psi_A(0)$, the $m = 0$ channel contributes. The Kondo coupling of the electrons with the impurity spin is given by

$$H_K = \frac{g}{2k_c^2} \sum_{s=1}^{N_s} \sum_{l=1}^{N_f} \sum_{\alpha, \beta=1}^{N_c} \sum_{a=1}^{N_c^2-1} \Psi_{l\alpha}^{s\dagger}(0) \tau_{\alpha\beta}^a \Psi_{l\beta}^s(0) S^a, \quad (59)$$

where g is the effective Kondo coupling for energy scales up to the cutoff Λ , \mathbf{S} denotes the spin at the impurity site, τ are the generators of the $\text{SU}(N_c)$ spin group, and we have now generalized the fermions, in the spirit of large N analysis, to have N_s flavors (valley indices) N_f colors (sublattice indices) and N_c spin. For realistic systems $N_f = N_c = N_s = 2$. Here we have chosen Kondo coupling g to be independent of sublattice and valley indices. This is not a necessary assumption. However, we shall avoid extension of our analysis to flavor and/or color dependent coupling term for simplicity. Also, the Dirac nature of the

graphene conduction electrons necessitates the Kondo Hamiltonian to mix $m = \pm 1$ and $m = 0$ channels (Eqs. 58 and 59). This is in complete contrast to the conventional Kondo systems where the Kondo coupling involves only $m = 0$ angular momentum channel.

The kinetic energy of the Dirac electrons can also be expressed in terms of the ξ fields:

$$H_0 = \int_0^\infty \frac{kdk}{2\pi} \sum_{m=-\infty}^\infty \sum_{s,\alpha} \left(E_+(k) \xi_{+\alpha}^{ms\dagger} \xi_{+\alpha}^{ms} + E_-(k) \xi_{-\alpha}^{ms\dagger} \xi_{-\alpha}^{ms} \right) \quad (60)$$

Typically such a term involves all angular momenta channels. For our purpose here, it will be enough to consider the contribution from electrons in the $m = 0, \pm 1$ channels which contribute to scattering from the impurity (Eqs. 58 and 59). To make further analytical progress, we now unfold the range of momenta k from $(0, \infty)$ to $(-\infty, \infty)$ by defining the fields $c_{1(2)\alpha}^s$

$$\begin{aligned} c_{1(2)\alpha}^s(k) &= \sqrt{|k|} \xi_{+\alpha}^{0(-\text{sgn}(s))s}(|k|), \quad k > 0, \\ c_{1(2)\alpha}^s(k) &= +(-) \sqrt{|k|} \xi_{-\alpha}^{0(-\text{sgn}(s))s}(|k|), \quad k < 0, \end{aligned} \quad (61)$$

so that one can express the Ψ fields as $\Psi_{A(B)\alpha}^s(0) = \int_{-\infty}^\infty \frac{dk}{2\pi} \sqrt{|k|} c_{1(2)\alpha}^s(k)$. In terms of the $c_{1(2)\alpha}^s$ fields, the kinetic energy (in the $m = 0, \pm 1$ channels) and the Kondo terms in the Hamiltonian can therefore be written as

$$\begin{aligned} H_0 &= \int_{-k_c}^{k_c} dk / (2\pi) E_k c_{l\alpha}^{s\dagger} c_{l\alpha}^s \\ H_K &= g / (8\pi^2 k_c^2) \int_{-k_c}^{k_c} \int_{-k_c}^{k_c} \sqrt{|k|} \sqrt{|k'|} dk dk' \\ &\quad \times \left(c_{l\alpha}^{s\dagger}(k) \tau_{\alpha\beta}^a c_{l\beta}^s(k') S^a \right), \end{aligned} \quad (62)$$

where $E_k = eV + \hbar v_F k$ and summation over all repeated indices are assumed.

We follow standard procedure⁴⁷ of representing the local spin by $\text{SU}(N_c)$ Fermionic fields f_α and write the partition function of the system in terms of the f and c fields

$$\begin{aligned} Z &= \int \mathcal{D}c \mathcal{D}c^\dagger \mathcal{D}f \mathcal{D}f^\dagger \mathcal{D}\epsilon e^{-S/\hbar}, \quad S = S_0 + S_1 + S_2 \\ S_0 &= \int_0^{\beta\hbar} d\tau \int_{-k_c}^{k_c} dk / (2\pi) \left(c_{l\alpha}^{s\dagger}(k, \tau) G_0^{-1} c_{l\alpha}^s(k, \tau) \right), \\ S_1 &= J / (4\pi^2 N_c k_c^2) \int_0^{\beta\hbar} d\tau \int_{-k_c}^{k_c} \int_{-k_c}^{k_c} \sqrt{|k|} \sqrt{|k'|} dk dk' \\ &\quad \times \left[c_{l\alpha}^{s\dagger}(k, \tau) \tau_{\alpha\beta}^a c_{l\beta}^s(k', \tau) f_\gamma^\dagger(\tau) \tau_{\gamma\delta}^a f_\delta(\tau) \right] \\ S_2 &= \int_0^{\beta\hbar} d\tau \left[(f_\alpha^\dagger(\tau) [\hbar \partial_\tau + \epsilon(\tau)] f_\alpha(\tau)) - \epsilon(\tau) Q \right], \end{aligned} \quad (63)$$

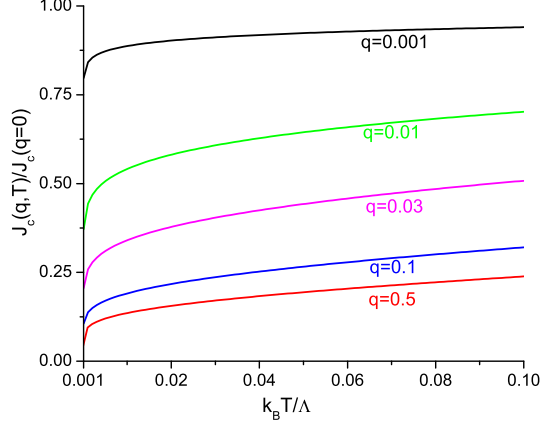


FIG. 15. Sketch of the critical Kondo coupling $J_c(q, T)$ as a function of temperature for several applied voltages $q = eV/\Lambda$. The Kondo phase exists for $J > J_c$.

where $G_0^{-1} = \hbar\partial_\tau + E_k$ is the propagator for c fields, $J = gN_c/2$ is the renormalized Kondo coupling, we have imposed the impurity site occupancy constraint $\sum_\alpha f_\alpha^\dagger f_\alpha = Q$ using a Lagrange multiplier field $\epsilon(\tau)$.

We now use the identity⁴⁷

$$\tau_{\alpha\beta}^a \tau_{\gamma\delta}^a = N_c \delta_{\alpha\delta} \delta_{\beta\gamma} - \delta_{\alpha\beta} \delta_{\gamma\delta} \quad (64)$$

and decouple S_1 using a Hubbard-Stratonovitch field ϕ_l^s . In the large N_c limit one has $S = S_0 + S_2 + S_3 + S_4$, where

$$\begin{aligned} S_3 &= \int_0^{\beta\hbar} d\tau \int_{-k_c}^{k_c} \frac{\sqrt{|k|} dk}{(2\pi)} \left(\phi_l^{*s}(\tau) c_{l\alpha}^{s\dagger}(k, \tau) f_\alpha(\tau) + \text{h.c.} \right) \\ S_4 &= N_c k_c^2 / J \int_0^{\beta\hbar} d\tau \phi_l^{*s}(\tau) \phi_l^s(\tau). \end{aligned} \quad (65)$$

Note that at the saddle point level $\langle \phi_l^s \rangle \sim \langle \sum_\alpha c_{l\alpha}^{s\dagger} f_\alpha \rangle$ so that a non-zero value of ϕ_l^s indicates the Kondo phase. In what follows, we are going to look for the static saddle point solution with $\phi_l^s(\tau) \equiv \phi_0$ and $\epsilon(\tau) \equiv \epsilon_0$ ⁴⁷. In this case, it is easy to integrate out the c and f fields, and obtain an effective action in terms of ϕ_0 and ϵ_0 and one gets $S' = S_5 + S_6$ with

$$\begin{aligned} S_5 &= -\beta\hbar N_c \text{Tr} [\ln (i\hbar\omega_n - \epsilon_0 - N_s N_f \phi_0^* G'_0(i\omega, V) \phi_0)], \\ S_6 &= \beta\hbar (N_s N_c N_f k_c^2 |\phi_0|^2 / J - \epsilon_0 Q), \end{aligned} \quad (66)$$

where Tr denotes Matsubara frequency sum as well as trace over all matrices and the Fermion Green function $G'_0(ip_n, q) \equiv G'_0$ is given by²⁷

$$G'_0 = \frac{-\Lambda}{2\pi(\hbar v_F)^2} (ip_n - q) \ln [1/|ip_n - q|^2], \quad (67)$$

where, in the last line we have switched to dimensionless variables $p_n = \hbar\omega_n/\Lambda$ and $q = eV/\Lambda$.

One can now obtain the saddle point equations from Eq. 66 which are given by $\delta S'/\delta\phi_0 = 0$ and $\delta S'/\delta\epsilon_0 = 0$. Using Eqs. 66 and 67, one gets (after continuing to real frequencies and for $T = 0$)

$$\begin{aligned} 1/J &= -\Lambda/(\pi\hbar v_F k_c^2)^2 \int_{-1}^0 dp G_0(p - \nu - \Delta_0 G_0/2)^{-1}, \\ Q/N_c &= 1/(2\pi) \int_{-1}^0 dp \nu(p - \nu - \Delta_0 G_0/2)^{-1}, \end{aligned} \quad (68)$$

where we have defined the dimensionless variable $\Delta_0 = N_f N_s |\phi_0|^2 / (\pi\hbar^2 v_F^2)$, $p = \hbar\omega/\Lambda$, $G_0 = 2\pi(\hbar v_F)^2 G'_0/\Lambda$, $\nu = \epsilon_0/\Lambda \geq 0$, and have used the energy cutoff Λ for all frequency integrals. At the critical value of the coupling strength, putting $\nu = 0$ and $\Delta_0 = 0$, we finally obtain the expression for $J_c(q, T)$

$$J_c(q, T) = J_c(0) [1 - 2q \ln(1/q^2) \ln(k_B T/\Lambda)]^{-1} \quad (69)$$

where the temperature $k_B T$ is the infrared cutoff, $J_c(0) = (\pi\hbar v_F k_c^2)^2/\Lambda = \pi^2\Lambda$ is the critical coupling in the absence of the gate voltage, and we have omitted all subleading non-divergent term which are not important for our purpose. For $V = 0 = q$, we thus have, analogous to the Kondo effect in flux phase systems²⁷, a finite critical Kondo coupling $J_c(0) = \pi^2\Lambda \simeq 20\text{eV}$ which is a consequence of vanishing density of states at the Fermi energy for Dirac electrons in graphene. Of course, the mean-field theory overestimates J_c . A quantitatively accurate estimate of J_c requires a more sophisticated analysis which we have not attempted here.

2. Results and Discussions

The presence of a gate voltage leads to a Fermi surface and consequently $J_c(q, T) \rightarrow 0$ as $T \rightarrow 0$. For a given experimental coupling $J < J_c(0)$ and temperature T , one can tune the gate voltage to enter a Kondo phase. Fig. 15, which shows a plot of $J_c(q, T)$ as a function of T for several gate voltages q illustrates this point. The temperature $T^*(q)$ below which the

system enters the Kondo phase for a physical coupling J can be obtained using $J_c(q, T^*) = J$ which yields

$$k_B T^* = \Lambda \exp \left[(1 - J_c(0)/J) / (2q \ln[1/q^2]) \right] \quad (70)$$

For a typical $J \simeq 2\text{eV}$ and voltage $eV \simeq 0.5\text{eV}$, $T^* \simeq 35\text{K}$ ⁶⁵ We stress that even with overestimated J_c , physically reasonable J leads to experimentally achievable T^* for a wide range of experimentally tunable gate voltages.

We now discuss the possible ground state in the Kondo phase qualitatively. In the absence of the gate voltage a finite J_c implies that the ground state will be non-Fermi liquid as also noted in Ref. 27 for flux phase systems. In view of the large J_c estimated above, it might be hard to realize such a state in undoped graphene. However, in the presence of the gate voltage, if the impurity atom generates a spin half moment and the Kondo coupling is independent of the valley(flavor) index, we shall have a realization of two-channel Kondo effect in graphene owing to the valley degeneracy of the Dirac electrons. This would again lead to overscreening and thus a non Fermi-liquid like ground state²⁶. The study of details of such a ground state necessitates an analysis beyond our large N mean-field theory. To our knowledge, such an analysis has not been undertaken for Kondo systems with angular momentum mixing. In this work, we shall be content with pointing out the possibility of such a multichannel Kondo effect in graphene and leave a more detailed analysis as an open problem for future work.

Next, we discuss experimental observability of the Kondo phenomena in graphene. The main problem in this respect is creation of local moment in graphene. There are several routes to solving this problem. i) Substitution of a carbon atom by a transition metal atom. This might in principle frustrate the strong sp^2 bonding and thus locally disturb the integrity of graphene atomic net. However, nature has found imaginative ways of incorporating transition metal atoms in p - π bonded planar molecular systems such as porphyrin⁴⁸. Similar transition metal atom incorporation in extended graphene, with the help of suitable bridging atoms, might be possible. ii) One can try chemisorption of transition metal atoms such as Fe on graphene surface through sp - d hybridization in a similar way as in intercalated graphite⁴⁹. iii) It might be possible to chemically bond molecules or free radicals with magnetic moment on graphene surface as recently done with cobalt phthalocyanene (CoPc) molecule on Au(111) surface⁵⁰. This might result in a strong coupling between graphene and impurity atom

leading to high Kondo temperatures as seen for CoPc on Au(111) surface ($T_K \simeq 280K$).
iv) Recently ferromagnetic cobalt atom clusters with sub nano-meter size, deposited on carbon nanotube, have exhibited Kondo resonance⁵¹. Similar clusters deposition in graphene might be a good candidate for realization of Kondo systems in graphene. v) From quantum chemistry arguments, a carbon vacancy, or substitution of a carbon atom by a boron or nitrogen might lead to a spin-half local moment formation. In particular, it has been shown that generation of local defects by proton irradiation can create local moments in graphite⁵². Similar irradiation technique may also work for graphene.

For spin one local moments and in the presence of sufficiently large voltage and low temperature, one can have a conventional Kondo effect in graphene. The Kondo temperature for this can be easily estimated using $k_B T_K \sim D \exp(-1/\rho J)$ where the band cutoff $D \simeq 10\text{eV}$, $J \simeq 2-3\text{eV}$ and DOS per site in graphene $\rho \simeq 1/20$ per eV. This yield $T_K \simeq 6-150K$. The estimated value of T_K has rather large variation due to exponential dependence on J . However, we note that Kondo effect due to Cobalt nano-particle in graphitic systems such as carbon nanotube leads to a high $T_K \approx 50K$ which means that a large J may not be uncommon in these systems. Recently, It has also been shown that the Kondo effect can be controlled by orbital degrees of freedom⁵³. A symmetry class of orbitals in a magnetic adatoms with inner shell in graphene leads to a distinct quantum critical points, where $T_K \propto (J - J_c)^{1/3}$ near the critical coupling J_c ⁵⁴.

Finally, we note that recent experiments have shown a striking conductance changes in carbon nanotubes and graphene, to the extent of being able to detect single paramagnetic spin-half NO_2 molecule⁵⁵. This has been ascribed to conductance increase arising from hole doping (one electron transfer from graphene to NO_2). Although Kondo effect can also lead to conductance changes, in view of the fact that a similar effect has been also seen for diamagnetic NH_3 molecules, the physics in these experiments is likely to be that of charge transfer and not local moment formation.

B. STM spectra of Graphene

The experimental situation for STM measurement is schematically represented in Fig. 16. The STM tip is placed atop the impurity and the tunneling current \mathcal{I} is measured as a function of applied bias voltage V . The possible positions of the impurity is shown in

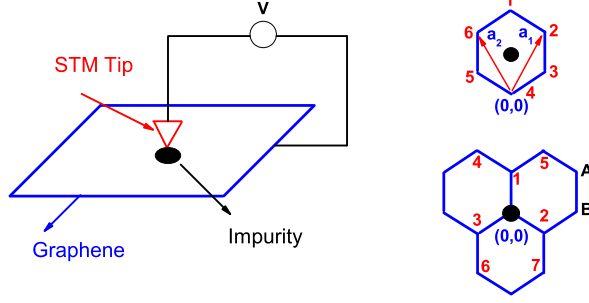


FIG. 16. Schematic experimental setup with the right panel showing two possible positions (atop hexagon center and atop a B site) of the impurity. The numbers denote nearest neighbor A and B sublattice sites to the impurity. $a_{1(2)} = +(-)\sqrt{3}/2\hat{x} + 3/2\hat{y}$ [lattice spacing set to unity] are graphene lattice vectors. The choice of coordinate center $(0,0)$ are shown for each case

the right panel of Fig. 16. Such a situation can be modeled by the well-known Anderson Hamiltonian⁵⁶. Here we incorporate the low-energy Dirac quasiparticles of graphene in this Hamiltonian which is given by

$$H = H_G + H_d + H_t + H_{Gd} + H_{Gt} + H_{dt} \quad (71)$$

$$H_G = \int_k \psi_s^{\beta\dagger}(\vec{k}) [\hbar v_F (\tau_z \sigma_x k_x + \sigma_y k_y) - E_F I] \psi_s^{\beta}(\vec{k})$$

$$H_d = \sum_{s=\uparrow,\downarrow} \epsilon_d d_s^\dagger d_s + U n_\uparrow n_\downarrow$$

$$H_t = \sum_\nu \left[\sum_{\sigma=\uparrow,\downarrow} \epsilon_{t\nu} t_{\nu s}^\dagger t_{\nu s} + (\Delta_0 t_{\nu\uparrow}^\dagger t_{-\nu\downarrow}^\dagger + \text{h.c.}) \right] \quad (72)$$

$$H_{Gd} = \sum_{\alpha=A,B} \int_k \left(V_\alpha^0(\vec{k}) c_{\alpha,s}^\beta(\vec{k}) d_s^\dagger + \text{h.c.} \right) \quad (73)$$

$$H_{dt} = \sum_{s=\uparrow,\downarrow;\nu} \left(W_\nu^0 t_{\nu s} d_s^\dagger + \text{h.c.} \right). \quad (74)$$

$$H_{Gt} = \sum_{\alpha=A,B;\nu} \int_k \left(U_{\alpha;\nu}^0(\vec{k}) c_{\alpha,s}^\beta(\vec{k}) t_{\nu s}^\dagger + \text{h.c.} \right) \quad (75)$$

Here H_G is the Dirac Hamiltonian for the graphene which are described by the two component annihilation operator $\psi_s^\beta(\vec{k}) = (c_{As}^\beta(\vec{k}), c_{Bs}^\beta(\vec{k}))$ belonging to the valley $\beta = K, K'$ and spin $s = \uparrow, \downarrow$, I is the identity matrix, τ and σ denotes Pauli matrices in valley and pseudospin spaces, v_F is the Fermi velocity, and $\int_k \equiv \sum_{\beta=K,K'} \sum_{s=\uparrow,\downarrow} \int \frac{d^2k}{(2\pi)^2}$. H_d denotes the impurity atom Hamiltonian with an on-site energy ϵ_d and U is the strength of on-

site Hubbard interaction. H_t is the Hamiltonian for the superconducting ($\Delta_0 \neq 0$) or metallic ($\Delta_0 = 0$) tip electrons with on-site energy $\epsilon_{t\nu}$ where ν signifies all quantum numbers (except spin) associated with the tip electrons. The operators d_s and $t_{\nu s}$ are the annihilation operators for the impurity and the tip electrons. The Hamiltonians H_{Gd} , H_{Gt} , and H_{dt} describe interaction between the graphene and the impurity electrons, the graphene and the STM tip electrons, and the impurity and the STM tip electrons respectively. The corresponding interactions parameters $V_\alpha^0(\vec{k})$, $U_{\alpha;\nu}^0(\vec{k})$, and W_ν^0 are taken to be independent of valley and spin indices of graphene electrons but may depend on their sublattice index or pseudospin. In defining the Hamiltonian Eq. 71, we omit inter-valley scattering of electrons by the impurity. This is usually justified if the impurity radius is larger than $|\vec{K} - \vec{K}'|^{-1}$ so that the inter-valley scattering is suppressed. In the present case, for impurity atom atop the hexagon center, the impurity scattering potential respects the pseudospin symmetry (since it does not distinguish between A or B sites) and hence can not flip pseudospin of graphene electrons. Thus a graphene electron in momentum state \vec{k}_1 around K valley can only be scattered to around momentum states $\vec{k}_2 = -\vec{k}_1$ in K' valley. This constraint further reduces the phase space for inter-valley scattering. This phase space constraint makes the inter-valley scattering small for all impurities atop hexagon center. For impurities atop graphene sites, our analysis is applicable for large impurity size where inter-valley scattering is negligible.

1. Tunneling Current

The tunneling current for the present model is given by

$$\mathcal{I}(t) = e\langle dN_t/dt \rangle = ie\langle [H, N_t] \rangle / \hbar \quad (76)$$

where $N = \sum_{\nu s} t_{\nu s}^\dagger t_{\nu s}$ is the number operator for the tip electrons. These commutators receive contribution from H_{dt} and H_{Gt} in Eqs. 74 and 75 and can be evaluated by a straightforward generalization of method outlined in Ref. 39 to the case of superconducting tips. A standard calculation yields

$$\begin{aligned} \mathcal{I} = \mathcal{I}_0 \int_{-\infty}^{\infty} d\omega [f(\omega - eV) - f(\omega)] \rho_t(\omega - eV) & \left[\rho_G(\omega) \right. \\ & \left. \times |U^0|^2 + \frac{|B(\omega)|^2}{\text{Im}\Sigma_d(\omega)} \frac{|q(\omega)|^2 - 1 + 2\text{Re}[q(\omega)]\chi(\omega)}{(1 + \chi^2(\omega))(1 + \xi^2)} \right] \end{aligned} \quad (77)$$

where $\mathcal{I}_0 = 2e(1 + \xi^2)/h$, $\rho_G(\epsilon)$ and $\rho_t(\epsilon)$ are the graphene and STM tip electron DOS respectively, $\xi = |U_B^0|/|U_A^0| = |V_B^0|/|V_A^0|$ is the ratio of coupling of the impurity to the electrons in B and A sites of graphene with $U_A^0 = U^0$ and $V_A^0 = V^0$, $\chi(\epsilon) = [\epsilon - \epsilon_d - \text{Re}\Sigma_d(\epsilon)]/\text{Im}\Sigma_d(\epsilon)$, $f(\epsilon) = 1/(1 + \exp[\epsilon/T])$ ($k_B = 1$) is the Fermi function, and $\Sigma_d(\epsilon)$ is the impurity advanced self-energy in the absence of the tip. Here $B(\epsilon) = V^0 U^0 I_2(\epsilon)$ and $q(\epsilon)$ is given by

$$q(\epsilon) = \frac{W^0/U^0 + V^0 I_1(\epsilon)}{V^0 I_2(\epsilon)} \quad (78)$$

where,

$$I_1(\epsilon) = (1 + \xi^2) \sum_k \text{Tr} [\text{Re}\{\mathcal{G}(\epsilon, \mathbf{k})\}] \quad (79)$$

$$I_2(\epsilon) = (1 + \xi^2) \sum_k \text{Tr} [\text{Im}\{\mathcal{G}(\epsilon, \mathbf{k})\}] \quad (80)$$

Here, we have neglected the energy dependence of the coupling functions assuming small applied voltages. Tr denotes trace over Pauli matrices in pseudospin, valley and spin spaces, and \mathcal{G} is the Green function for the graphene electrons:

$$\mathcal{G}(\epsilon, \mathbf{k}) = \frac{(\epsilon + E_F)I - \hbar v_F(\tau_z \sigma_x k_x + \sigma_y k_y)}{(\epsilon + E_F)^2 - \hbar^2 v_F^2 |\mathbf{k}|^2 - i\eta} \quad (81)$$

A simple calculation yields^{39,57}

$$\begin{aligned} I_1(\epsilon) &= -4(1 + \xi^2)(\epsilon + E_F) \ln |1 - \Lambda^2/(\epsilon + E_F)^2| / \Lambda^2 \\ I_2(\epsilon) &= 4(1 + \xi^2)\pi |\epsilon + E_F| \theta(\Lambda - \epsilon - E_F) / \Lambda^2. \end{aligned} \quad (82)$$

where Λ is the ultraviolet momentum cutoff and θ is the Heaviside step function. Usually, in graphene, Λ is taken to be the energy at which the graphene bands start bending rendering the low-energy Dirac theory inapplicable and can be estimated to be $1 - 2\text{eV}$ ³¹.

2. Results and Discussions

Here we are going to analyse the tunneling conductance $G = \frac{dI}{dV}$ as measured by STM. In the absence of impurities, the contribution to the conductance comes from the first term of Eq. 77. For s-wave superconducting tips, one finds that the tunneling conductance

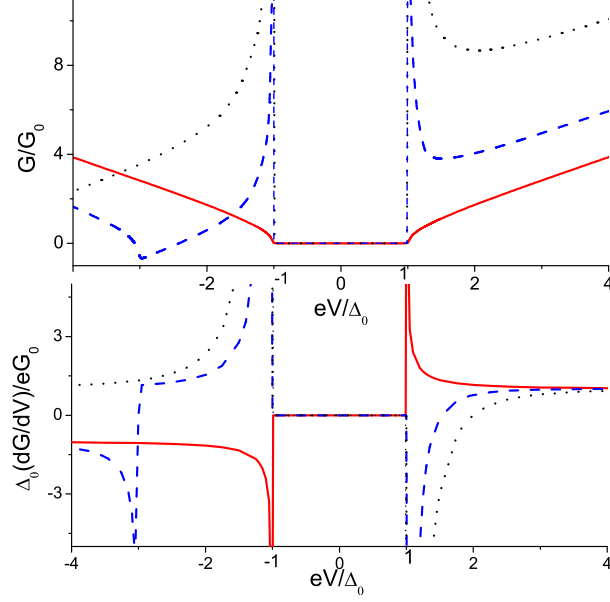


FIG. 17. (Color online) Plot of the tunneling conductance G and its derivative dG/dV as a function of the applied bias voltage $eV/\Delta_0 = -p$ for $r = 0, 2, 6$ (red solid, blue dashed and black dotted lines) respectively. See text for details.

($G(V) = d\mathcal{I}/dV$) for $E_F > 0$ and at $T = 0$ is given by (with $r = E_F/\Delta_0$, $p = -eV/\Delta_0$)

$$G = G_0 \left[\mathcal{N}_t(p)|r| + \int_p \text{Sgn}(z - p + r) \mathcal{N}_t(z) dz \right] \quad (83)$$

$$\frac{dG}{dV} = \frac{eG_0}{\Delta_0} \left[\mathcal{N}_t(p) - \mathcal{N}'_t(p)|r| - 2\theta(p - r)\mathcal{N}_t(p - r) \right] \quad (84)$$

where $G_0 = 8\pi^2 e^2 |U^0|^2 (1 + \xi^2) \rho_{0t} \rho_0 / h$, $\rho_G = \rho_0 |r - p|$, $\rho_t(r) = \rho_{0t} \mathcal{N}_t(r)$, $\mathcal{N}_t(x) = |x|/\sqrt{x^2 - 1} \theta(|x| - 1)$, and $\text{Sgn}(x)$ denote the signum function. For graphene with $E_F = r = 0$, $dG/dV \sim \text{Sgn}(V) \mathcal{N}_t(-V)$, *i.e.*, the tip DOS is given by the derivative of the tunneling conductance. For large E_F away from the Dirac point, the first term of G becomes large and reflects the tip DOS. In between these extremes, when $E_F \sim eV$, neither G nor dG/dV reflects the DOS. In this region, the signature of the Dirac point appears through a cusp (discontinuity) in G (dG/dV) at $eV = -E_F - \Delta_0$ arising from the contribution of the second (third) term in Eq. 83 (Eq. 84). These features, shown in Fig. 17, distinguishes such graphene STM spectra with their conventional counterparts⁴⁰.

Next, we turn to the case of impurity doped graphene and consider a metallic tip with constant DOS. The contribution to the tunneling conductance from the impurity (after

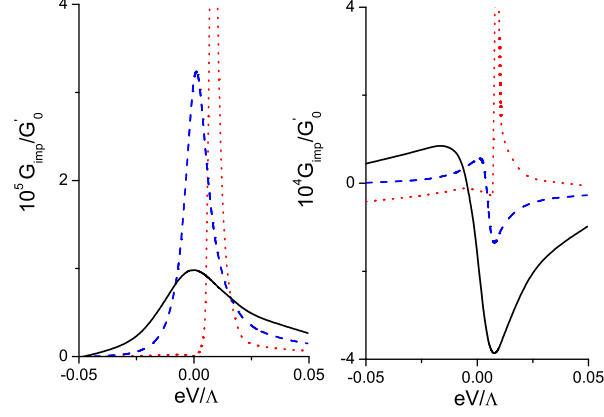


FIG. 18. (Color online) Plot of G_{imp} as a function of V for $|W^0/U^0| = 0.05$ (right; impurity atop a site) and 2 (left; impurity atop hexagon center) for $E_F/\Lambda = 0.3, 0.1$, and 0 (black solid, blue dashed and red dotted lines respectively). Plot parameters are $5U = V^0 = 0.05\Lambda$, $W^0 = 0.0005\Lambda$, and $\epsilon_d = 0$.

subtracting the graphene background) at $T = 0$ (Eq. 82) is

$$G_{\text{imp}} = G'_0 \frac{|B(V)|^2}{\text{Im}\Sigma_d(V)} \frac{|q(V)|^2 - 1 + 2\text{Re}[q(V)]\chi(V)}{\Lambda[1 + \chi^2(V)]}, \quad (85)$$

where $G'_0 = 2e^2\rho_{0t}\Lambda/h$. Such tunneling conductances are known to have peak/antiresonance/dip feature at zero bias for $|q| \gg 1/\simeq 1/\ll 1$ ³⁸. In conventional metals, Eq. 77 can be used to compute the STM current by taking U^0 as a fixed parameter independent of the position of the impurity. However, the situation in graphene necessitates a closer attention to U^0 which is proportional to the probability amplitude of the Dirac quasiparticles in graphene to hop to the tip. The strength of U^0 can be estimated using the well-known Bardeen tunneling formula⁵⁸:

$$U^0 \sim \int d^2r \left(\phi_\nu^\dagger(z) \partial_z \Psi_G(\vec{r}, z) - \Psi_G^\dagger(\vec{r}, z) \partial_z \phi_\nu(z) \right) \sim \Psi_G(\vec{r}_0, z_0) \quad (86)$$

where the last similarity is obtained by a careful evaluation of the surface integral $\int d^2r$ over a surface between the graphene and the tip parallel to the graphene sheet⁵⁹, (\vec{r}_0, z_0) is the coordinate of the tip center⁵⁹, $\phi_\nu(z)$ is tip electron wavefunction, and the wavefunction graphene electrons $\Psi_G(\vec{r}, z)$ around $K(K')$ valley, can be written, within tight-binding

approximation, as⁶⁰

$$\begin{aligned} \Psi_G(\vec{r}, z) = \frac{1}{\sqrt{N}} \sum_{\vec{R}_i^A} e^{i[\{\vec{K}(\vec{K}') + \delta\vec{k}\} \cdot \vec{R}_i^A]} & \left[\varphi(\vec{r} - \vec{R}_i^A) \right. \\ & \left. + e^{+(-)i\theta_k} \varphi(\vec{r} - \vec{R}_i^B) \right] f(z). \end{aligned} \quad (87)$$

Here $\theta_k = \arctan(k_y/k_x)$, $\delta\vec{k}$ is the Fermi wave-vector as measured from the Dirac points with $|\delta\vec{k}| \ll |\vec{K}(\vec{K}')|$ for all E_F , $\varphi(\vec{r})$ are localized p_z orbital wavefunctions, N is a normalization constant, $f(z)$ is a decaying function of z with decay length set by work function of graphene, and $\vec{R}_i^{A(B)} = n\hat{a}_1 + m\hat{a}_2(\hat{a}_2 - \hat{y})$ with integers n, m denote coordinates of the graphene lattice sites (Fig. 16)⁶⁰. When the impurity and the STM tip is atop the center of the hexagon, pseudospin symmetry necessitates $\varphi(\vec{r}_0 - \vec{R}_i^{A,B})$ to be identical for all neighboring A and B sublattice points 1.6 surrounding the impurity (Fig. 16). Consequently, the sum over lattice vectors \vec{R}_i^A in Eq. 87 reduces to a sum over the phase factors $\exp(i[\{\vec{K}(\vec{K}') + \delta\vec{k}\} \cdot \vec{R}_i^A])$ for these lattice points. It is easy to check that this sum vanishes for both Dirac points (when $|\delta\vec{k}| = 0$). Thus the only contribution to $\Psi_G(\vec{r}_0, z_0)$ comes from the second and further neighbor sites for which the amplitude of localized wavefunctions $\varphi(\vec{r}_0 - \vec{R}_i^{A/B})$ are small. For finite E_F , ($\delta\vec{k} \neq 0$) there is a finite but small contribution ($O(|\delta\vec{k}|/|\vec{K}|)$) to $\Psi_G(\vec{r}_0, z_0)$ from the nearest neighbor sites. Thus $\Psi_G(\vec{r}_0, z_0)$ and hence U^0 is drastically reduced when the impurity is atop the hexagon center. In this case, we expect $U^0 \ll W^0$ and hence $|q| \gg 1$ (Eq. 78) leading to a peaked spectra for all E_F . In contrast, for the impurity atom atop a site, there is no such symmetry induced cancellation and $\psi_G(\vec{r}_0, z_0)$ receives maximal contribution from the nearest graphene site directly below the tip. Thus we expect $|U^0| \gg |W^0|$ (since it is easier for the tip electrons to tunnel to delocalized graphene band than to a localized impurity level) leading to $q \simeq I_1/I_2 \simeq -\ln|1 - \Lambda^2/(eV + E_F)^2|/\pi$. For large $|eV + E_F|$ and impurity atop a site, $q \leq 1$ leading to a dip or an antiresonance in G_{imp} which is qualitatively distinct from the peaked spectra for impurity atop the hexagon center. As $E_F \rightarrow 0$, q diverges logarithmically for small eV . However, it can be shown that in this regime χ shows a stronger linear divergence for $eV \neq \epsilon_d$ which suppresses G_{imp} . At $eV = \epsilon_d$, the divergence of χ also becomes logarithmic and we expect a peak of G_{imp} . Note that these effects are independent of Σ_d and hence of the precise nature of the impurity. Such an impurity position dependent peak/dip structure of G_{imp} has been observed for magnetic impurities in Ref. 35 for $E_F \gg eV$.

To demonstrate this feature, we restrict ourselves to impurities with small Hubbard U and compute the self energy of the impurity electrons within a mean-field theory where $Un_\sigma n_{\bar{\sigma}} = U\langle n_\sigma \rangle n_{\bar{\sigma}}$ leading to spin-dependent on-site impurity energy $\epsilon_\sigma = \epsilon_d + U\langle n_{\bar{\sigma}} \rangle$ ⁵⁷. Using Eqs. 71 and 73, one then obtains the mean-field advanced impurity Green function $\mathcal{G}_\sigma^{\text{imp}}(\omega) = (\omega - \epsilon_\sigma - \Sigma_d(\omega))^{-1}$ where the impurity self-energy is given by $\Sigma_d(\omega) = |V^0|^2(I_1 + iI_2)$ and mean-field self-consistency condition demands $n_\sigma = \int d\omega/\pi \text{Im}\mathcal{G}_\sigma^{\text{imp}}(\omega)$. Following Ref. 57, we solve these equations to get $\chi(\epsilon)$, and $\text{Im}\Sigma_d(\epsilon)$ which can be substituted in Eq. 85 to obtain G_{imp} . We note, from Eqs. 85 and 78, that G_{imp}/G'_0 depends on the ratios E_F/Λ , V^0/Λ , and W^0/U^0 which can not be quantitatively determined from the Dirac-Anderson model. We therefore treat them as parameters of the theory and compute G_{imp} for their representative values as shown in Fig. 18. In accordance with earlier discussions, we find that for large $E_F/\Lambda = 0.3$, G_{imp} has qualitatively different features; for the impurity at the center of the hexagon, it shows a peak (left panel) while for that atop a site (right panel), it shows a dip. The change of G_{imp} from a dip to a peak via an antiresonance as a function of E_F/Λ when the impurity is atop a site can be seen from right panel of Fig. 18. In contrast, the left panel always shows peak spectra.

Before ending this section, we note that the logarithmic divergence of the G_{imp} when the impurity is reasonably close to the Dirac point is a characteristics of the Dirac physics of the low-energy quasiparticles. This feature is therefore also expected to be seen for tunneling conductance measured atop an impurity on the surface of a topological insulator.

V. CONCLUSION

In this review we have presented a theory for transport properties across superconducting junctions of graphene with barriers of thickness d_0 and arbitrary gate voltages V_0 applied across the barrier region. The oscillatory behaviour of the tunneling conductance as well as Josephson current are shown to be robust even for a barrier of finite width. In the thin barrier limit, such behavior is the manifestation of the transmission resonance of DBdG quasiparticles in superconducting graphene. Graphene is an interesting candidate for transport applications, in particular for spintronics as it exhibits remarkably high mobility with easily controllable carrier density. Superconducting junctions of graphene has recently been realized experimentally^{42,46}. Further experiments in this direction may therefore lead

to realization of SBS and NBS junctions discussed in this review and hence may lead to verification of some the theoretical results discussed here.

The effect of localized impurities on the electronic properties of graphene has attracted a lot of recent attention. We have studied the effect of presence of localized magnetic impurities in graphene which gives rise to the Kondo effect i.e. the dynamic screening of the localized moment. The Kondo effect in graphene is unconventional as the effective coupling Kondo coupling strength (for weak coupling regime) can be tuned by gate voltage. Recent studies⁵⁴ have found that the Kondo coupling strength can also be controlled by a gate voltage in the strong coupling regime. We also discuss scanning tunneling conductance spectra phenomenon for both doped and undoped graphene. The position of the impurity on or in graphene plays a subtle role and affects the underlying physics of STM spectra in doped graphene. For impurity atoms atop the hexagon center, the zero-bias tunneling conductance shows a peak; for those atop a graphene site, it shows a dip. This feature is a direct consequence of pseudospin symmetry and Dirac nature of graphene quasiparticles. A recent scanning tunneling microscopy (STM) experiment⁶¹ has demonstrated the ability to controllably ionize individual Co adatom on graphene using either a back gate voltage or the STM tip bias voltage. This has opened up the possibility of probing the interesting electronic phenomena which arises due to the interplay of the impurity with the graphene electrons.

We thank I. Paul and S. Bhattacharjee for collaboration on related topics. K.S thanks DST for support through grant SR/S2/CMP-001/2009.

¹ K. S. Novoselov, A. K. Geim, S. V. Morozov, D. Jiang, Y. Zhang, S. V. Dubonos, I. V. Grigorieva, and A. A. Firsov, *Science* **306**, 666 (2004).

² P. R. Wallace, *Phys. Rev.*, **71**, 622-634 (1947).

³ T. Ando, *J. Phys. Soc. Jpn.* **74** 777 (2005).

⁴ V. P. Gusynin and S. G. Sharapov, *Phys. Rev. Lett.* **95**, 146801 (2005); N. M. R Peres, F. Guinea, and A. H. Castro Neto, *Phys. Rev. B* **73**, 125411 (2006); V. Lukose, R. Shankar and G. Baskaran, *Phys. Rev. Lett.*, **98** 116802 (2007).

⁵ K. S. Novoselov, A. K. Geim, S. V. Morozov, D. Jiang, M. I. Katsnelson, I. V. Grigorieva, S.

- V. Dubonos, and A. A. Firsov, *Nature* **438**, 197 (2005); K. S. Novoselov, E. McCann, S. V. Morozov, V. I. Falko, M. I. Katsnelson, U. Zeitler, D. Jiang, F. Schedin, and A. K. Geim, *Nat. Phys.* **2** 177 (2006).
- ⁶ M. I. Katsnelson, K. S. Novoselov and A. K. Geim, *Nat. Phys.*, **2**, 620 (2006)
- ⁷ O. Klein, *Z. Phys.*, **53**, 157 (1929).
- ⁸ A. H Castro Neto, F. Guinea, N. M. R Peres and A. K Geim *Rev. Mod. Phys.*, **81**, 109 (2009).
- ⁹ C. W. J Beenakker, *Rev. of Mod. Phys.*, **80**, 1337 (2008).
- ¹⁰ N. M. R Peres, *Rev. Mod. Phys.*, **82**, 2673 (2010); S. Das Sarma, S. Adam, E. H. Hwang and E. Rossi, *Rev. Mod. Phys.*, **83**, 407 (2011).
- ¹¹ C. W. J. Beenakker, *Phys. Rev. Lett.*, **97**, 067007 (2006).
- ¹² A. F. Volkov, P. H. C. Magnee, B. J. van Wees, and T. M. Klapwijk, *Physica C*, **261**, 242 (1995).
- ¹³ M. Titov, C. W. J. Beenakker, *Phys. Rev. B.*, **74**, 041401(R) (2006).
- ¹⁴ B. Uchoa, A. H. Castro Neto, *Phys. Rev. Lett.*, **98**, 146801 (2007)
- ¹⁵ A.F. Andreev *Sov. Phys. JETP* **19**, 1228 (1964).
- ¹⁶ G.E. Blonder, M. Tinkham, and T. M. Klapwijk, *Phys. Rev. B* **25**, 4515 (1982).
- ¹⁷ S. Bhattacharjee, K. Sengupta, *Phys. Rev. Lett.*, **97**, 217001 (2006)
- ¹⁸ S. Bhattacharjee, M. Maiti and K. Sengupta, *Phys. Rev. B*, (76), 184514 (2007)
- ¹⁹ M. Maiti, K. Sengupta, *Phys. Rev. B*, **76**, 054513 (2007)
- ²⁰ K. K. Likharev, *Rev. Mod. Phys.* **51**, 101 (1979).
- ²¹ A. A. Golubov, M. Y. Kupryanov, and E. Il'ichev, *Rev. Mod. Phys.* **76**, 411 (2004).
- ²² I.O. Kulik and A. Omelyanchuk, *JETP Lett.* **21**, 96(1975); *ibid* *Sov. Phys. JETP* **41**, 1071 (1975).
- ²³ V. Ambegaokar and S. Baratoff, *Phys. Rev. Lett.* **10**, 486, (1963).
- ²⁴ See for example A.C. Hewson *The Kondo Problem to Heavy Fermions*, Cambridge University Press (1993).
- ²⁵ M. Pustilnik and L. Glazman, *J. Phys. Condens. Matter*, **16** R 513 (2004).
- ²⁶ For a review see I. Affleck, *Acta Phys. Polon.* **B26** 1869 (1995); cond-mat/9512099.
- ²⁷ C. R. Cassanello and E. Fradkin *Phys. Rev. B* **53**, 15079 (1996); D. Withoff and E. Fradkin, *Phys. Rev. Lett* **64**, 1835 (1990); K. Insegerent, *Phys. Rev. B* **54**, 11396 (1996).
- ²⁸ A. Polkovnikov, S. Sachdev and M. Vojta, *Phys. Rev. Lett* **86**, 296 (2001).
- ²⁹ A. Furusaki and N. Nagaosa, *Phys. Rev. Lett* **72**, 892 (1994).

- ³⁰ S. Saremi and P.A. Lee, Phys. Rev. B **75**, 165110 (2007).
- ³¹ K. Sengupta and G. Baskaran, Phys. Rev. B **77**, 045417 (2008).
- ³² M. Hentschel and F. Guinea, *Phys. Rev. B*, **76**, 115407 (2007)
- ³³ K. Saha, I. Paul, K. Sengupta, Phys. Rev. B, 165446 (2010).
- ³⁴ B. Uchoa, L. Yang, S. W. Tsai, N. M. R. Peres, and A. H. Castro Neto, Phys. Rev. Letters **103**, 206804 (2009).
- ³⁵ H. Manoharan (private communication).
- ³⁶ I. Brihuega, P. Mallet, C. Bena, S. Bose, C. Michaelis, L. Vitali, F. Varchon, L. Magaud, K. Kern, and J. Y. Veuillen, Phys. Rev. Lett **101**, 206802 (2008).
- ³⁷ T. Valla, A. V. Fedorov, Jinho Lee, J. C. Davis, and G. D. Gu, Science **314**, 1914 (2006); see, e.g., O. Fischer, M. Kugler, I. Maggio-Aprile, C. Berthod, and C. Renner, Rev. Mod. Phys. **79**, 353 (2007).
- ³⁸ U. Fano, Phys. Rev **124** 1866 (1961); V. Madhavan, W. Chen, T. Jamneala, M. F. Crommie, and N. S. Wingreen, Science **280**, 567 (1998).
- ³⁹ Y. Meir and N. S. Wingreen, Phys. Rev. Lett **68**, 2512 (1992); Y. Meir, N. S. Wingreen, and P.A. Lee, Phys. Rev. Lett **70**, 2601 (1993).
- ⁴⁰ S. H. Pan, E. W. Hudson, and J. C. Davis, Appl. Phys. Lett. **73**, 2992 (1998); A. Kohen, Th. Proslier, T. Cren, Y. Noat, W. Sacks, H. Berger, and D. Roditchev, Phys. Rev. Lett. **97**, 027001 (2006); I. Guillaumon, H. Suderow, S. Vieira, and P. Rodiere, Physica C **468**, 537 (2008).
- ⁴¹ Y. Zhang, Y. -W. Tan, H. L. Stormer, and P. Kim, Nature **438**, 201 (2005);
- ⁴² H. Heersche et. al., *Nature*, **446**, 56 (2007).
- ⁴³ A. M. Zagoskin *Quantum Theory of Many Body Systems*, Springer-Verlag, New York (1998).
- ⁴⁴ H-J. Kohn, K. Sengupta and V.M. Yakovenko, Eur. Phys. J. B **37**, 349 (2004).
- ⁴⁵ P. W. Anderson and J. Rowel, Phys. Rev. Lett. **10**, 230 (1963).
- ⁴⁶ Du, X., I. Skachko, and E. Y. Andrei, 2008, Phys. Rev. B **77**, 184507.
- ⁴⁷ N. Read and C.J. Newns, J. Phys. C **16**, 3273 (1983).
- ⁴⁸ Porphyrin Hand Book, Eds. K. M. Kadish, K.M. Smith and R. Guilard, (Academic Press, New York) 1999.
- ⁴⁹ M. E. Vol'pin and Yu. N. Novikov, Pure and Appl. Chem., vol. **60**, No. 8, 1133 (1988)
- ⁵⁰ A. Zhao, Q. Li, L. Chen, H. Xiang, W. Wang, S. Pan, B. Wang, X. Xiao, J. Yang, J. G. Hou, and Q. Zhu, Science **309**. 1542 (2005).

- ⁵¹ T. W. Odom, J.-L. Huang, C. L. Cheung, and C. M. Lieber, *Science*, **290** 1459 (2000)
- ⁵² P. O. Lehtinen, A. S. Foster, Yuchen Ma, A. V. Krasheninnikov, and R. M. Nieminen, *Phys. Rev. Lett* **93**, 187202 (2004).
- ⁵³ T. O. Wehling, A. V. Balatsky, M. I. Katsnelson, A. I. Lichtenstein, and A. Rosch, *Phys. Rev. B* **81**, 115427 (2010).
- ⁵⁴ B. Uchoa, T. G. Rappoport, and A. H. Castro Neto, *Phys. Rev. Lett.* **106**, 016801 (2011).
- ⁵⁵ T. O. Wehling, K. S. Novoselov, S. V. Morozov, E. E. Vdovin, M. I. Katsnelson, A. K. Geim, A. I. Lichtenstein, *Nano Lett.* **8**; 173-177 (2008); S. Adam, S. Das Sarma and A. K. Geim, *Phys. Rev. B* **76**, 195421 (2007).
- ⁵⁶ P.W. Anderson *Phys. Rev.* **124** 41 (1961).
- ⁵⁷ B. Uchoa, V. N. Kotov, N. M. R. Peres and A. H. Castro Neto, *Phys. Rev. Lett* **101**, 026805 (2008).
- ⁵⁸ J. Bardeen, *Phys. Rev. Lett* **6**, 57 (1961).
- ⁵⁹ J. Tersoff and D. R. Hamann, *Phys. Rev. Lett* **50**, 1998 (1983).
- ⁶⁰ C. Bena and G. Montambaux, *New J. Phys.* **11**, 095003 (2009).
- ⁶¹ V. W. Brar, R. Decker, H.-M. Solowan, Y. Wang, L. Maserati, K. T. Chan, H. Lee, C. O. Girit, A. Zettl, S. G. Louie, Marvin L. Cohen, and M. F. Crommie, *Nature Physics*, **7**, 43 (2011).
- ⁶² Since our solution for the wavefunction at the barrier region breaks down at $V_0 = E_F$, it is necessary to carefully analyze the limit $V_0 \rightarrow E_F$ for arriving at this conclusion.
- ⁶³ Note that at $V_0 = E_F$, $\alpha_c = 0$ leading to $G = 0$. Thus the divergence of periodicity do not constitute a physical singularity.
- ⁶⁴ For short junctions ($d \ll \xi$), the main contribution to the Josephson current comes from the subgap states.¹³.
- ⁶⁵ Note that J in our analysis is an effective coupling valid below the scale Λ *i.e.* $J > J_{\text{bare}}$. This might further enhance T^* .